Title

Irreversibility at macromolecular scales in the flake graphite of the lithium-ion battery anode.

Authors

Lodico, Jared J
Lai, Chun-Han
Woodall, Mark
et al.

Publication Date

2019-10-01

DOI

10.1016/j.jpowsour.2019.226841

Peer reviewed

Irreversibility at macromolecular scales in the flake graphite of the lithium-ion battery anode

Jared J. Lodico,[1,2] Chun-Han Lai,[3] Mark Woodall,[1,2] Ho Leung Chan,[1,2]
Erick Garcia,[1,2] William A. Hubbard,[1,2] Bruce Dunn,[3] and B. C. Regan[1,2,*]

[1] *Department of Physics and Astronomy, University of California, Los Angeles, CA 90095, U.S.A.*
[2] *California NanoSystems Institute, University of California, Los Angeles, CA 90095, U.S.A.*
[3] *Department of Materials Science and Engineering, University of California, Los Angeles, California 90095 USA*

Charging a commercial lithium-ion battery intercalates lithium into the graphite-based anode, creating various lithium carbide structures. Despite their economic importance, these structures and the dynamics of their charging-discharging transitions are not well-understood. We have videoed single microcrystals of high-quality, natural graphite undergoing multiple lithiation-delithiation cycles. Because the equilibrium lithium-carbide compounds corresponding to full, half, and one-third charge are gold, red, and blue respectively, video observations give direct insight into both the macromolecular structures and the kinematics of charging and discharging. We find that the transport during the first lithiation is slow and orderly, and follows the core-shell or shrinking annuli model with phase boundaries moving at constant velocities (i.e. non-diffusively). Subsequent lithiations are markedly different, showing transport that is both faster and disorderly, which indicates that the initially pristine graphite is irreversibly and considerably altered during the first cycle. In all cases deintercalation is not the time-reverse of intercalation. These findings both illustrate how lithium enters nearly defect-free host material, and highlight the differences between the idealized case and an actual, cycling graphite anode.

I. INTRODUCTION

Lithium-ion batteries are currently the preferred power source for portable applications ranging from cell phones and laptop computers to electric automobiles and trucks. Despite their near ubiquity, the operation of Li-ion batteries (LIBs) is not well understood at the macromolecular level,[1,2] which hampers efforts to further improve the technology. Of the three essential components – the anode, cathode, and electrolyte – the anode has the chemistry that is perhaps the most settled, with graphite the usual material of choice.[1,3,4] Compared to the alternatives, graphite has a moderate specific charge (372 mAh/g) and practical rate capability (∼2 C charge and 20 C discharge),[5] but – crucially – it returns to a good approximation of its original shape even after hundreds of charge-discharge cycles. In fact, the advantages of graphite are compelling enough that dual-carbon cells have even been considered, where graphite serves as both the anode material and the cathode material.[6]

Carbon-based LIB anode materials include amorphous carbons, both hard and soft, and graphite, both synthetic and natural. Of the four, natural graphite has the largest capacity, but it must be charged the most slowly.[7] In terms of energy density, power density, service life, and safety, the graphites have the most balanced profile and thus by far the largest market share (89% in 2016).[7,8] Natural (flake) and synthetic graphite nearly split the market, with natural graphite preferred for its lower cost and synthetic graphite preferred for its slightly larger charging rate.[8] Much recent work has been devoted to improving, through morphological or chemical modifications, the rate performance of natural flake graphite.[9,10] Given the compelling advantages (and market relevance) of natural graphite as an anode material, and the interest in improving its rate capacity to accommodate fast-charge applications,[8,9] a fundamental study of the physical transport mechanisms governing the lithiation of natural graphite is timely.

The present understanding of the lithiation process, and of the lithium carbide compounds occurring in Li-ion batteries is surprisingly poor. For instance, the half-reaction occurring at the negative electrode (anode), the intercalation or deintercalation of lithium into graphite, is known to produce ordered lithium carbide with well-defined "staging". A "stage n" intercalation compound has n graphene layers separating each pair of intercalant layers. The lithium-graphite intercalation compound (GIC) that occurs in a fully charged Li-ion battery, LiC_6, is stage 1. Removing half of the lithium gives LiC_{12}, which is stage 2. At present, while the structure of the fully intercalated LiC_6 is known, the three-dimensional structure of LiC_{12} is not (see below), to say nothing of the kinematics of the transitions between stages.[2] Understanding how lithium intercalates and deintercalates graphite is an essential part of understanding how current Li-ion batteries function, and how future rechargeable batteries can be improved.

In a defect-free crystal, lithium is thought to enter the host lattice strictly from the edges, in the directions perpendicular to the c-axis.[11,12] Initially the lithium inserts uniformly between all the graphene planes, forming a dilute stage 1, or 1', GIC.[13] Once between the planes, the lithium is thought to move via diffusion.[11,12] With continuing intercalation the density of the lithium becomes high enough that an effective lithium-lithium interaction acts to organize the initially independent, 2D lithium gases, first enforcing the staging, inter-plane crys-

tallization, and then at the highest densities (or low temperature) an intra-plane crystallization. Staging,[14] as observed with in situ X-ray diffraction, has been reported for n as high as 8.[2] At room temperature the most lithium-rich phases, LiC_6 and LiC_{12}, are ordered in all three dimensions, showing the same intra-plane crystallization at stage 1 and stage 2 respectively.[15] The next-most-lithium-rich phase, 2L, is also stage 2,[3] but more dilute and disordered or "liquidlike" in plane,[13] with a formula of LiC_{18},[2,15] though see Ref. 3. However, for both the stage 2 and stage 2L phases, the inter-plane ordering is thought to require that the lithium in a gallery between two graphene planes be organized into distinct islands, and that these islands stack, layer to-layer, to form domains. Daumas and Herold[16] postulated the existence of these domains in an attempt to provide a physically reasonable picture of staging transitions, which, within this theory, are accomplished by reorganization of the islands within each layer. Neither the size of these domains in any n>1 GIC, nor their reconfiguration kinematics during a stage transition, are presently known.[17]

Despite its limited spatial resolution, optical microscopy has the potential to reveal important aspects of the kinematics of graphite (de)lithiation. As in many GICs,[18] distinct colors are associated with particular lithium carbide stoichiometries.[19] LiC_6 is gold, LiC_{12} is red (also described as pink or copper-colored), and the stage 2L compound LiC_{18} is blue.[15,20] Thus it is possible to optically identify a GIC's state of charge (SOC),[19,21–25] and to observe the propagation of reaction fronts through an extended graphite electrode.[21,23,25–29] As we will see, it is also possible to directly visualize aspects of the standard model of intercalation, such as whether (1) lithium enters a graphite crystallite from the sides, (2) moves via diffusion, and (3) forms staged compounds in correspondence with the GIC's SOC.

To take advantage of this correspondence between color and stoichiometry, we have videoed the lithiation and delithiation of single microcrystals of high-quality, natural flake graphite over many charge/discharge cycles (Figure 1). Natural graphite is customarily classified into three grades: vein, flake, and amorphous, with flake graphite serving as the raw material for natural graphite-based LIB anodes.[8,10,30] After processing (micronizing), this graphite is reduced to roughly 20 μm diameter spherical microcrystals.[7] Our flakes are comparably sized in two dimensions, but only a few hundred nanometers thick. Because the lithium intercalates from the edges only, this form factor effectively provides a cross-sectional view of the interior of a microcrystal like those used in the LIB anode.

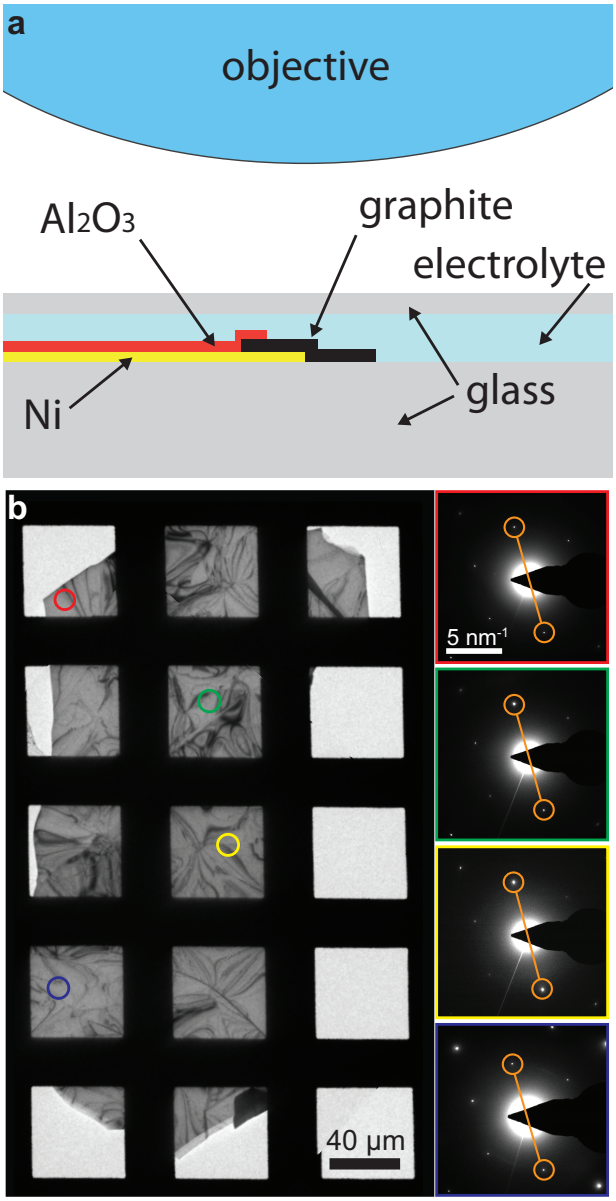

Figure 1. (a) A mechanically exfoliated graphite flake is electrically connected to a pre-patterned nickel electrode that is mostly encapsulated by aluminum oxide (Al_2O_3) to suppress background reactions. Two glass slides (top slide thickness ~150 μm) sandwich the graphite and electrolyte (1M $LiClO_4$ in EC:DMC). (See Figure S1, S2, and Methods for detailed description of experimental procedure.) Lithium foil (not shown) is used for both the reference and counter electrodes. (b) Bright field TEM image of a typical graphite flake on a lacey carbon copper grid. Select area diffraction from randomly selected regions (colored circles, ~80 μm^2) give substantially identical patterns (opposing peaks highlighted in orange), indicating that the flake is a single crystal.

II. RESULTS

An overview of a typical experiment, where a single graphite microcrystal on a metal electrode is lithiated and delithiated repeatedly, is given in Figure 2 (see also

Figure S2). The flake's basal plane is imaged, with the flake's c-axis parallel to the direction of observation. Optical microscopy shows the flake changing from its native grey color to yellow-gold and back (Figure 2a-c) through the first three complete cycles (for the next five cycles see Figure S3). Here, the graphite is cycled from the open circuit potential (OCP) to 5 mV at a rate of 1 mV/s, held at a constant voltage (CV) of 5 mV for 3.5 hours, and then returned to the OCP at a rate of 0.5 mV/s. Thus a voltage ramp replaces the constant current (CC) phase of the CCCV[31] charging protocol used for both standard and fast charging. Relative to CC, the voltage ramp gives superior predictability when testing small, individual graphite flakes whose electrochemistry might not dominate the parasitic chemistry on, e.g., the metal electrode. These scanning conditions were chosen to minimize degradation of the graphite[32] and to represent fast[31] but not extreme charging conditions. Full charge occurs in about an hour, while the max current of 15 nA, sustained, would lithiate the flake in 10 minutes. Thus the effective C-rate is in the range 1 to 6 C.

Color changes are associated with the electrical current, with the most dramatic changes occurring after the peak negative current and before the peak positive current (Figure 2d). After the first cycle the flake's coloring becomes very reproducible, reliably cycling back and forth between its native grey and the golden color indicative of full intercalation (Figures 2 and S3). The flake's basic morphology is unchanged from cycle to cycle, although defects appear during the very first lithiation. The number and apparent intensity of these defects, which show a prevalence of 120° and 60° angles indicative of the underlying hexagonal crystal lattice, increase with repeated cycling (see Figure S3 and Movie S1). The nickel electrode extending from the bottom right of the image does not change color or appear otherwise altered. Similarly, the solid electrolyte interphase (SEI) is not visible, which is as expected since the EC:DMC electrolyte is known to form a high quality SEI that is only a few nanometers thick.[7]

Close inspection reveals that the flake's first lithiation is unlike the ones that follow. During this first half-cycle the colors are clearly advancing from the edges, in some places as well-defined waves that develop into a grey-blue-red-gold progression moving toward the center of the flake. However, only slight vestiges of this behavior are evident in the second cycle, and for the third and subsequent cycles (see Figure S3) the flake's color changes are both delocalized and less dramatic. The flake changes color uniformly, with no marked distinction between the edge and the center. After a slight blue shift, the entire flake transitions to gold via a goldish-grey as it lithiates, without the clear blues and reds seen in the waves of the first half-cycle.

The color evolution of a flake during delithiation is also unexpectedly different from that seen during lithiation: the former is not the time reverse of the latter (Figure 2a-c). During delithiation, the initially golden flake passes through phases that are roughly uniform across the entire flake, showing first strong reds and then equally vibrant blues before returning to its native grey. These bright colors are not evident during lithiation, except as the localized waves appearing in the singular first half-cycle discussed previously. The correspondence between stoichiometry, or, equivalently, SOC, and color is evidently not one-to-one: depending on a graphite flake's charge history, identical lithium content could be indicated by bands of blue, red, and gold, a uniform red, or a uniform greyish-gold. Clearly, at intermediate SOC, a given amount of lithium can be organized within the graphite's crystal lattice in more than one way, and these different structures have different optical reflectivities.

The singular nature of the first lithiation is more marked in some cases. Figure 3 shows five frames selected from a video of a different graphite crystal's first electrochemical intercalation. (To give a sense of scale, this crystal is roughly 23 μm × 220 μm, and thus has a width comparable to that of the ∼20 μm graphite particles "typical" to a LIB anode.[7] See Figure S2.) In the second and third frames the flake has changed color relative to its initial state with such speed that the subtle color boundaries (which we take to be indicative of phase boundaries[26,28]) are difficult to note in the still images (see Movie S2 for a better perspective). However, the fourth frame clearly shows the co-existence of the blue, red, and gold phases. As the lithium-rich phases appear first on at the edge of the crystal, and then move steadily toward the center, this single image represents a compelling confirmation of a core-shell[33] or shrinking annuli[5] model of the graphite intercalation process (for the first half-cycle only), with lithium insertion occurring solely at the graphite microcrystal's edge planes. Of the four different graphite microcrystals reported here (see Figures 2-3 and S2-S7), all show the coexistence of three phases at some point during the first cycle, though not generally with fully continuous shrinking annuli. Because this Figure 3 flake presents the most regular and well-ordered first intercalation, we believe that it most closely approximates the ideal of a defect-free, single crystal lying flat on a smooth substrate.

Plotting the position of various phase boundaries as a function of time (Figure 3b) reveals that these boundaries move with constant velocities.[33,34] This first-lithiation behavior was seen consistently in every sample observed, regardless of crystallite shape or thickness (see Figure S4). In this sample the velocities measured span more than two orders of magnitude, with the red-to-gold phase boundary moving 300 times slower than an observed phase boundary between two unidentified dilute phases. The velocity magnitude depends on the type of boundary (e.g. red-blue), but here is roughly independent of the location within the crystal, as is evident from the uniform widths of the red and gold rings seen in Figure 3a(iv). As the lithium content increases, the phase boundary movement becomes more obviously directed from the edge toward the center, and becomes slower

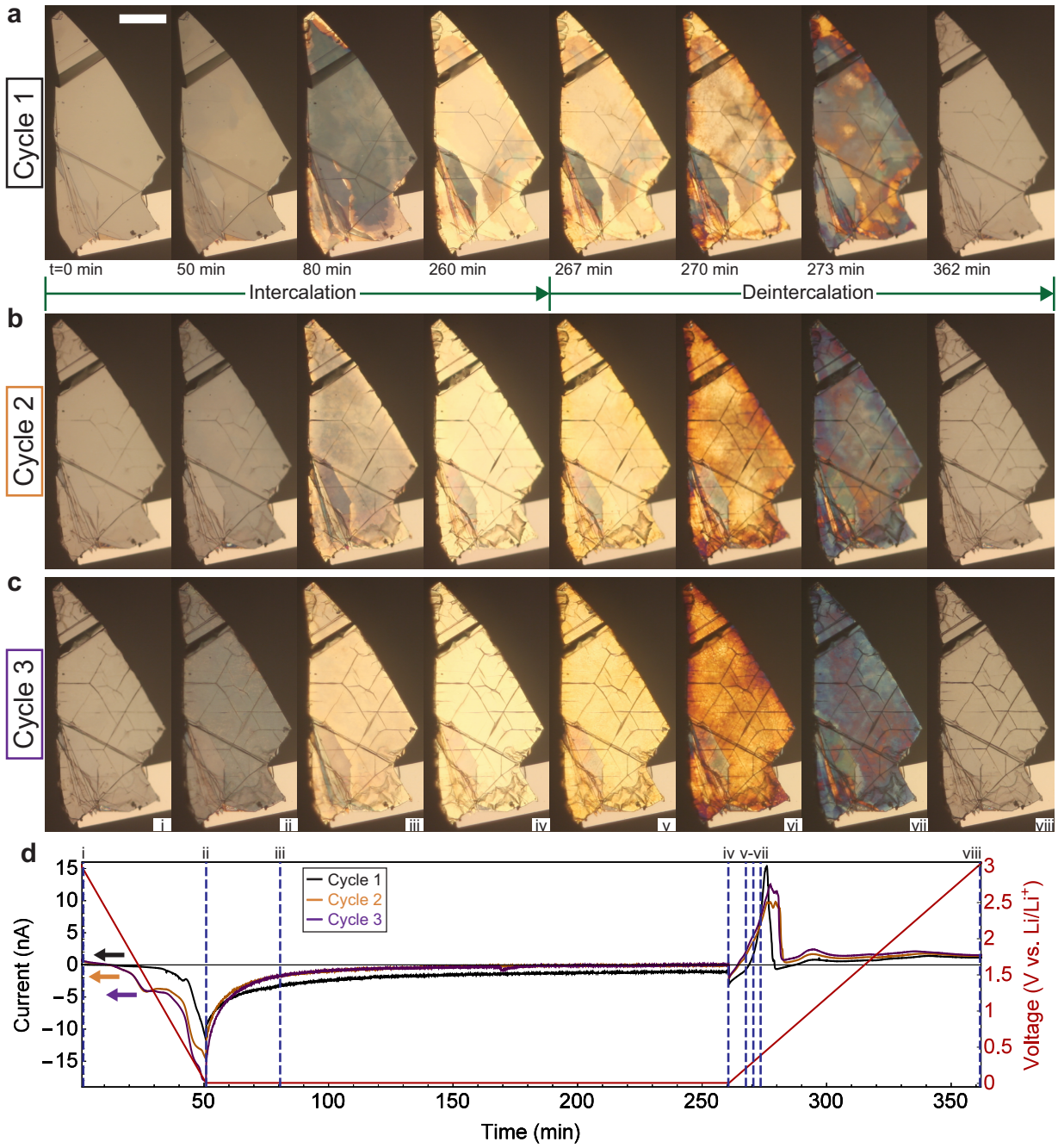

Figure 2. (a-c) Unprocessed images from the first three intercalation/deintercalation cycles. The flake is 170 nm thick, and the scale bar is 50 μm. (d) Current (color indicated) and voltage (in red) vs. time for the intercalation/deintercalation cycles shown in (a-c). The blue dashed lines in (d) labeled with Roman numerals indicate when each column of images in (a-c) was acquired, modulo the cycle number. (See Movie S1.)

(see Figure S8).[5] For instance, before the blue phase is achieved, the phase boundaries move sufficiently quickly that a given boundary is only visible for a few frames (images were acquired at a rate of one per 20 s), and only two phases are present in the crystal at a given moment. But, at the instant captured in Figure 3a(iv), the red phase has not yet obliterated the blue phase when the gold phase is already appearing behind it.

The simultaneous co-existence of the three phases not only gives a measure of the dramatic departure from equilibrium, perhaps not expected in such a small (23 μm wide) crystal that has been held at a constant electri-

cal potential for more than 10 minutes, but also rules out an underlying reason: insufficient lithium. (Three phase co-existence has been previously observed with optical methods.[23,24,26–29]) Without this image, one might reasonably wonder whether the "slow" intercalation (i.e. failure to reach quasi-equilibrium) was caused by insufficient Li diffusion through the electrolyte to the microcrystal edge. However, Figure 3a(iv) presents clear evidence of a surfeit of lithium within the graphite with respect to the blue-to-red phase transition, since the transition from red to an even more lithium-rich phase (gold) is being driven simultaneously. Evidently the rate limiting step for the blue-to-red transition is both (a) internal to the graphite and (b) not simple (Fickian) diffusive transport within the graphite, since the wave-front positions scale with the time t, and not $\sqrt{t}$.[27,28,33,34] In other words, while the main mass transport occurs via long-range diffusion, the phase transformation is "civilian" (as opposed to "military") and rate-controlled by the physics at the phase boundary, as in condensation or evaporation.[35] Similar constant-velocity wavefronts have been observed previously, but with 100× worse spatial resolution, and interpreted in terms of diffusion.[23] Here the revelatory power of video observations is manifest, for distinguishing diffusive from moving-boundary transport is difficult with electrochemical transport data alone.[33,34] The physical mechanism limiting this transition is likely rate-limiting for the other phase transitions of the first half-cycle, given the consistency of the linear behavior for all the observed phase transitions. Interestingly, this reasoning also indicates that the limiting mechanism is effective regardless of the particulars of the lithium-organization process underway, whether it be interlayer staging (transitioning to the blue phase 2L), intra-plane crystallization (blue phase 2L to red stage 2), or the final filling (red stage 2 to gold stage 1).

Our qualitative observations about the color evolutions of a graphite flake undergoing electrochemical cycling can be made more quantitative by plotting the trajectories in color space. We work in the CIE $L^*a^*b^*$ color space which, unlike the camera's native red-green-blue (RGB) format, is both device-independent and designed to give a faithful representation of human visual perception. Roughly speaking, the L^* coordinate describes the lightness on a black-to-white scale, while the orthogonal a^* and b^* coordinates give the color in terms of opposing components red-green and yellow-blue respectively.[36] (For RGB channel values for the graphite flake in Figure 3 during the first lithiation cycle, see Figures S9 and S10.)

As noted earlier, during the first lithiation half-cycle, color waves propagate from the crystal edge toward its center, with multiple colors visible simultaneously. During delithiation the flake also shows distinct reds and blues, but much more uniformly. This behavior is made evident by plotting the color, in the three-dimensional $L^*a^*b^*$ space, of every pixel in a given ROI for the various lithiation states (Figure 4). We also plot the color path of a single, representative pixel to serve as a guide for visualizing a typical color trajectory (see Figure S11). During the first cycle both the lithiation and delithiation paths deviate from the direct path between the grey and gold endpoints. The larger deviation of the delithiation paths is indicative of more vibrant colors. On cycles after the first, a graphite crystal's color moves directly from grey to gold during lithiation, and in a roundabout trajectory through even more vibrant reds and blues during delithiation. (See Movie S2 for a dynamic view.)

From these observations we can draw several immediate conclusions. First, the color changes observed in graphite during lithiation are not a function of the level of charge doping alone, for in one dimension there is only one path, and here we see that even a small area of graphite will take a different color path intercalating than it does deintercalating. A Drude model where the GIC's optical conductivity depends only on the lithium concentration is overly simplistic[27] – the structure and organization of the lithium dopants must also be important. Since X-ray data has shown that the colors of lithium GICs indicate ordered staging, and the trajectory endpoints (fully intercalated and deintercalated) are well-ordered, the most reasonable deduction is that the greyish-gold colored lithium compounds observed during intercalation correspond to disordered, unstaged (or solid solution[3,26]) GICs, at least on the $\gtrsim 1$ μm length scales resolvable in this experiment. In the arguments that follow we adopt this assumption.

During the first cycle the lithium transport within the graphite host is not diffusion limited, contrary to the usual assumption. Since the colored phases represent staged compounds, the lithium intercalation transport during the first cycle is evidently orderly (reds and blues) and slow (several visible reaction fronts), but not diffusion-limited (constant velocity wavefronts). In subsequent cycles the intercalation transport is faster (crystal color is homogeneous) and disorderly (only greyish gold). Surprisingly, despite the faster intercalation transport during cycles after the first, the system is less successful at reaching the thermodynamically-preferred, ordered intermediate (blue and red) phases. However, it does reach the fully lithiated endpoint (gold) phase faster (roughly 4× faster in the third cycle compared to the first).[11] Deintercalation is faster than intercalation: the transport is orderly (bright colors) and, at times, rate limiting (color gradients are evident across a flake – see Figures S3 and S5).

We have written a simulation that shows, in cross-section, the kinematics of intercalation and deintercalation implied by the optical data for the various cycles (Figure 5 and Movie S5). The existence or absence of color variations – and the implied phase separation – across the microcrystals constrains the physical models. The colors themselves give a direct measure of organization of the lithium along c-axis of the graphite at the scale of single and double graphene layers, where the graphite layer repeat distance is 0.335 nm.[14]

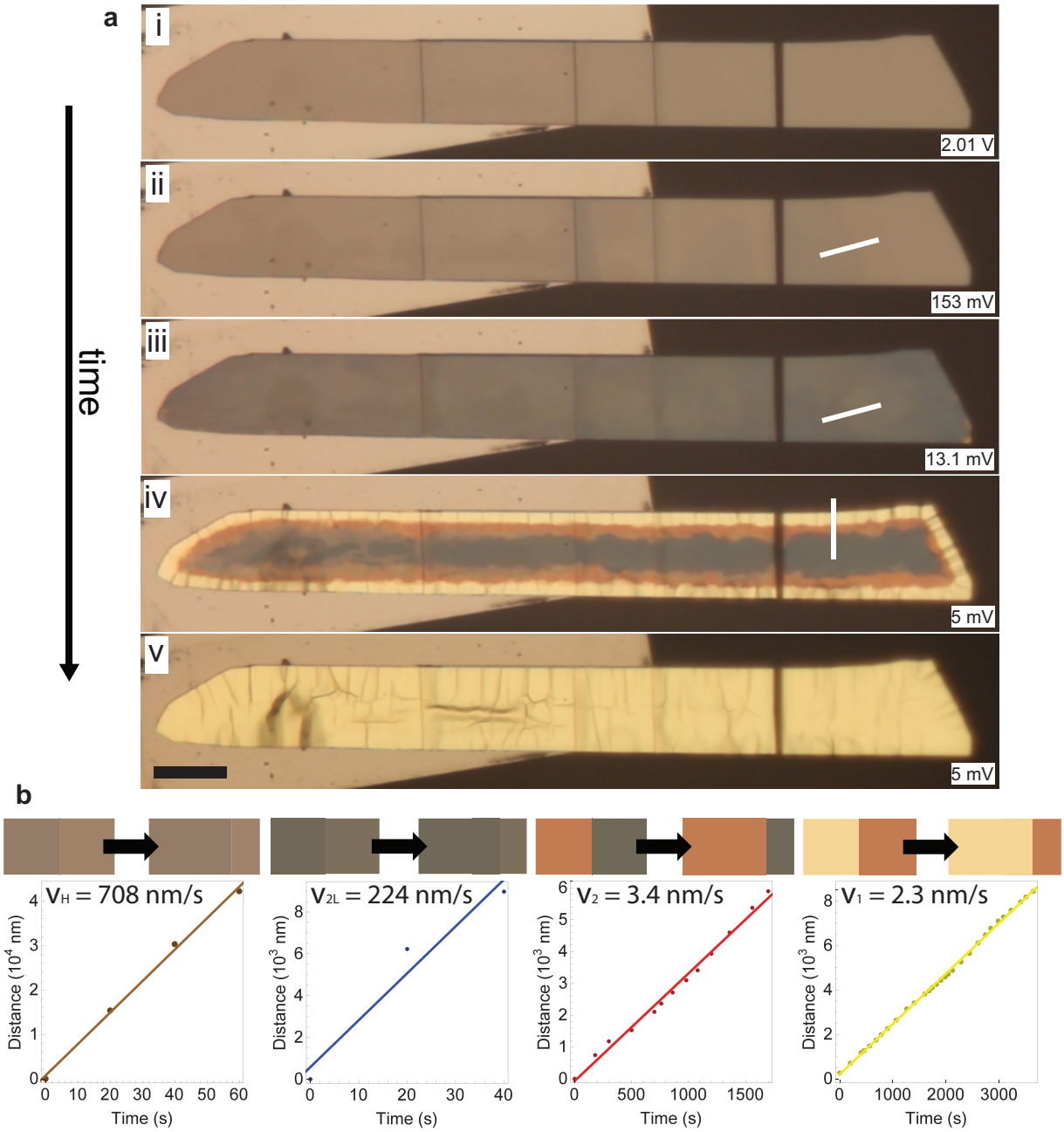

Figure 3. (a) A 180 nm thick graphite flake during its first lithiation. Here, time is increasing from top to bottom. Frames i, ii, and iii were acquired at 2.01 V, 153 mV, and 13.1 mV, while ramping at 1 mV/s as in Figure 2. Frames iv, and v were acquired 14 and 93 minutes into the hold at 5 mV. (b) Position vs. time plots for different color transitions, acquired at the locations indicated by the white lines in (a). The scale bar is 20 μm. (See Movie S2 and Figure S10 for the entire cycle.)

Duplicating the homogeneous[37] intercalation behavior observed for cycles after the first is straightforward, requiring only random motion of the lithium ions that is fast compared to the ratio of the crystal size to the timescale of the Li-ion concentration changes (Figure 5d). Reproducing the inhomogeneous, staged behavior of the first intercalation half-cycle (Figure 5a), which clearly shows wavefronts at low stages, and the deintercalation half-cycles (Figures 5b and 5c), which show (comparatively) little evidence of concentration gradients, is more challenging. For the former case, first intercalation, we have chosen to show a model featuring intercalant moving at constant velocity, which easily shows waves and DH domains, but does not allow for phase boundaries moving at different velocities. An alternative model (not shown), based on random ion motion with energy advan-

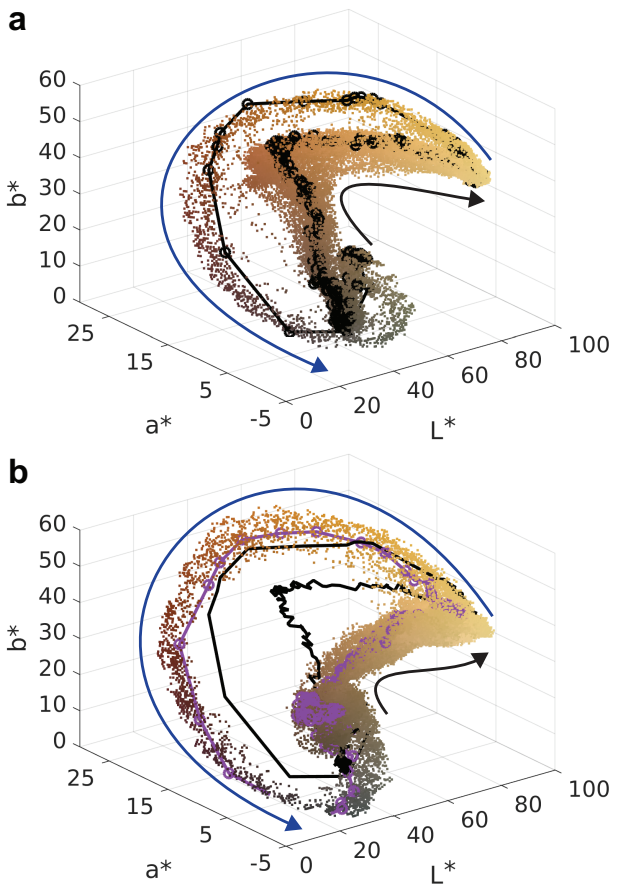

Figure 4. L*a*b* color space plots of a region of interest (ROI) during cycle 1 (a) and 3 (b) from the sample in Figure 3 and Movie S2. Every pixel in a 50 pixel × 20 pixel ROI from frames 0 to 1100 (a) and 1281 to 2381 (b) is indicated with a colored dot. For each cycle the path of one representative pixel from this ROI (see Figure S11) is highlighted, with the black path from (a) shown again in (b). The path direction during the intercalation and subsequent deintercalation is indicated by black and blue arrows respectively.

tages and penalties assigned based on the occupation of neighboring galleries, gives some staging and wavefront velocities that differ from stage to stage, but is disinclined to produce DH domains. For the latter case, deintercalation, we show a 'nested staircase' model that faithfully gives a crystal-spanning, uniform ion concentration (on length scales larger than the domain size), with staging and without phase separation. On the other hand, it also gives staircase velocities that are proportional to the distance from a central, motionless staircase, which places an upper bound on how large a defect-less area showing such coordinated motion could be. Interestingly, the nested staircase model implies 'inverted' staging (Figure 5b), which would have an X-ray diffraction signature that would distinguish this model from one based on phase separation,[13] which we do not see here.

The models shown in these kinematic simulations are meant to be illustrative of our data. Developing dynamical models that are physically reasonable (i.e. that include, for example, solvent effects and avoid intercalant teleportation[27]) and reproduce the data is clearly a formidable task,[4,12,38,39] with much room for future improvement. This task is beyond the scope of the present work.

III. DISCUSSION

A consistent picture emerges from the data presented. The first lithiation proceeds in waves representing phases of steadily increasing lithium content that propagate with constant velocity from the edge of an ideal graphite crystallite toward its center. The wave velocities range from >500 nms for the most dilute phases to about 5 nm/s for the red-to-gold phase transition. Subsequent lithiations, especially after the second cycle, show no wave fronts, and change from grey to gold with little sign of other colors. Delithiation, on the other hand, again especially after the second cycle, gives bright reds and blues that appear uniformly throughout the crystallite.

We interpret these observations as follows. The initial structure of the graphite flake is known: nearly defect-free, single crystal, AB-stacked graphite.[14] The lithiation behavior from this known state is entirely different from the lithiation behavior observed in all of the lithiations subsequent to the first one. Clearly the first lithiation/delithiation cycle irreversibly alters the structure of the graphite from its initial, pristine state. Despite the appearances presented by our optical images, which show no gross structural modifications and only a moderate increase in defect density, at the end of the first cycle the graphite is not returning to anything like a good approximation of its initial structure. The differences are sufficiently profound so as to completely alter the transport dynamics of the lithium intercalation. To correctly model lithium carbide during the characteristic (post-first-cycle) operation of a Li-ion battery,[4] especially when starting from first principles,[12,38,39] evidently one must account for deviations from the ideal, crystalline graphite host. In addition to the visible defects introduced during the first lithiation, unobserved, submicroscopic defects or crystallographic changes could also be playing a critical role. The nature of these lithiation-induced structural changes is not presently clear. Definitively identifying, e.g. incipient exfoliation, wrinkles, puckering, or microcracks,[14] will require the use of additional imaging techniques.

The marked distinction between the intercalation and deintercalation processes has been seen previously using other experimental methods.[3,5,22,26,34] For instance, galvanostatic intermittent titration was used to identify a delay in the $LiC_{12} \rightarrow LiC_6$ transformation, which was attributed to a slow nucleation step in the creation of the lithium-rich phase.[34] (In the reverse process, the generation of lithium "holes" does not require nucleation and

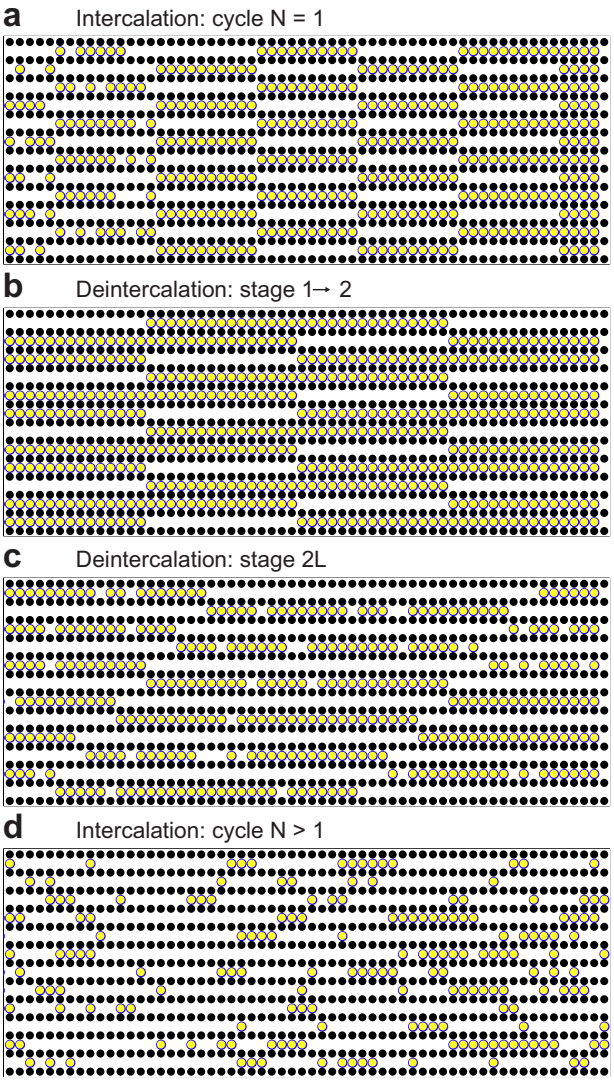

Figure 5. Four snapshots from a computer simulation (see Movie S5) showing the intercalation kinematics in cross-section. The black and yellow circles represent carbon and lithium respectively. (a) First intercalation cycle, showing intercalation from right to left with three phases visible: stage 2L, stage 2, and stage 1. (b) Deintercalation, spatially uniform across the crystal, showing an intermediate phase, or 'inverted stage', between stage 1 and stage 2 that has as its repeating unit two full layers followed by an empty one. (c) Deintercalation, subsequent to that shown in (b), which is also spatially uniform and shows stage 2L. (d) Intercalation as seen in cycles after the first, where no organization, either horizontal or vertical, is evident and the graphite goes directly from stage 1' to stage 1.

proceeds without delay.) In another example, ex situ optical observations of opened Li-ion cells revealed color differences, which persisted regardless of waiting time, between charging and discharging anodes at the same SOC.[22]

The data presented here illustrate the complex nature of lithium transport within crystalline graphite, and highlight the dangers of attempting to describe this transport with a simple (e.g. diffusion) model. For intercalation during the first cycle, for instance, the concentration profile implied by the multiple color rings propagating from the edge toward the center of the crystallite (see Figure 3a(iv) and the supplementary information) is inconsistent with simple diffusion.[5] In other words, a staircase-like concentration profile (see Figures S9 and S12) with sharp ($\lesssim$ 1 μm) steps separated by long ($\gtrsim$ 5 μm) plateaus does not represent a solution to Fick's second law with a constant diffusion coefficient D.[4,5,33] We are assuming here that, for instance, the gold and red phases are uniform, stoichiometric LiC_6 and $Li_{0.5}C_6$, and that an optically unresolved concentration gradient exists at the phase boundary. (See supplementary information.) An alternative possibility is that concentration gradients exist throughout the optically uniform gold and red phases, with a step discontinuity occurring in the optical properties at some intermediate stoichiometry (e.g. $Li_{0.75}C_6$).[23,24]

Relative to the 20 μm spherical graphite particle "typical" of a LIB anode, the single crystals presented here are much thinner along the c-axis, and comparably-sized-to-broader in the basal plane (see Figure S2 caption). However, because we find constant-velocity wave propagation during the first intercalation and uniform intercalation otherwise, our results are scale invariant over the size regime of interest. Our optical resolution is $\lesssim$ 1 μm and the largest flake dimension studied is $\sim$250 μm. Our observations thus indicate that lithium transport is constant-velocity for the first and uniform for subsequent intercalations for particles of any size within this 1 – 250 μm regime, which easily spans the entirety of the range of relevance for LIB anodes.

In summary, we have presented optical video, transport data, and a computer simulation of the intercalation of graphite microcrystals by lithium over multiple charge-discharge cycles at high C-rates. During the first lithiation, when the graphite host begins in a high-quality, crystalline state, constant-velocity waves of different ordered lithium-carbide phases propagate from a crystallite's edges towards its center. The more lithium-rich phases exhibit slower wavefront velocities. During subsequent lithiations, the transport is faster and does not show ordered intermediate phases with defined wavefronts. Delithiation is not the time-reverse of lithiation: as it deintercalates, the graphite shows brighter, crystal-spanning colors, indicating fast transport with ordered staging and without phase separation. Overall the data presented provide vivid support for the core-shell or shrinking annuli models – during the first intercalation – and highlight the importance of phase nucleation. Equally clear, however, is that the first intercalation irreversibly alters the structure of the graphite host. Thus the macromolecular structure of a graphite anode under operational conditions in a cycling lithium ion battery is only poorly approximated by ideal, crystalline graphite;

a graphite structure deformed by wrinkles, puckering, or incipient exfoliation, for example, might be more accurate. The singular transport and accompanying structural modifications of the first lithiation suggest how a specially-tailored first- charge protocol implemented during the manufacture of lithium-ion batteries might contribute to optimizing subsequent battery performance. By demonstrating the various modes – and corresponding rates – of charge transport and the causative structural changes in the natural flake graphite of the Li-ion battery anode, these findings contribute to the development of next-generation, fast charging batteries for automotive and other applications.

IV. METHODS

Single crystal graphite was mechanically exfoliated from bulk natural flake graphite (NGS Naturagraphit GmBH) and transferred to a nickel electrode on a glass slide (Figure 1) through a new pipette-drop transfer technique (see Figure S1). Flake thickness was measured with a Bruker NT9300 optical profiler. To minimize its parasitic contribution to the transport data,[17,28] the nickel electrode was encased in 18 nm of aluminum oxide (Al_2O_3) deposited via atomic layer deposition (ALD) (see Figure S2). A 1M lithium perchlorate ($LiClO_4$) solution in ethylene carbonate (EC):dimethyl carbonate (DMC) (1:1 by volume) served as the electrolyte. Lithium perchlorate was chosen over the currently preferred salt for commercial LIBs, lithium hexafluorophosphate ($LiPF_6$), because $LiPF_6$ is known to produce toxic and highly-reactive HF when exposed to even ppm concentrations of water.[40] The three-electrode experiments were assembled and conducted at room temperature in an argon atmosphere at ambient pressure, using a Gamry Reference 600 for electrochemical control. Before every experiment the electrolyte was "conditioned" by cycling the working electrode potential at 4 mV/s between the OCP and 1 V vs. Li/Li^+ several times to reduce the amount of parasitic chemistry present during the actual experiment. Image acquisition was performed with a Canon T3i consumer-grade digital camera on a Mitutoyo FS60 upright microscope. Lighting was provided by a standard, fiber coupled halogen lamp (EKE, nominal 150 W powered with 82 W DC). All images in this paper are presented with their original, as-acquired coloring, and without any digital enhancement or filtering.[24,28] Transmission electron microscopy (TEM) data were acquired in a FEI Titan 80-300 S/TEM operated at 80 kV with a 30 pA beam current (spot 8, 50 μm C2 aperture).

ACKNOWLEDGMENTS

This work was supported by National Science Foundation (NSF) Grant No. DMR-1611036, and by STROBE, an NSF STC under Grant No. DMR-1548924. The authors acknowledge the use of instruments at the Nano and Pico Characterization Lab at the CNSI at UCLA.

* regan@physics.ucla.edu

[1] V. A. Sethuraman, L. J. Hardwick, V. Srinivasan, and R. Kostecki, "Surface structural disordering in graphite upon lithium intercalation/deintercalation," *Journal of Power Sources*, vol. 195, pp. 3655–3660, June 2010.

[2] T. Ohzuku, Y. Iwakoshi, and K. Sawai, "Formation of Lithium-Graphite Intercalation Compounds in Nonaqueous Electrolytes and Their Application as a Negative Electrode for a Lithium Ion (Shuttlecock) Cell," *Journal of The Electrochemical Society*, vol. 140, pp. 2490–2498, Sept. 1993.

[3] A. Senyshyn, O. Dolotko, M. J. Mühlbauer, K. Nikolowski, H. Fuess, and H. Ehrenberg, "Lithium Intercalation into Graphitic Carbons Revisited: Experimental Evidence for Twisted Bilayer Behavior," *Journal of The Electrochemical Society*, vol. 160, pp. A3198–A3205, Jan. 2013.

[4] M. Park, X. Zhang, M. Chung, G. B. Less, and A. M. Sastry, "A review of conduction phenomena in Li-ion batteries," *Journal of Power Sources*, vol. 195, pp. 7904–7929, Dec. 2010.

[5] M. Heß and P. Novák, "Shrinking annuli mechanism and stage-dependent rate capability of thin-layer graphite electrodes for lithium-ion batteries," *Electrochimica Acta*, vol. 106, pp. 149–158, Sept. 2013.

[6] J. A. Seel and J. R. Dahn, "Electrochemical Intercalation of PF6 into Graphite," *Journal of The Electrochemical Society*, vol. 147, pp. 892–898, Mar. 2000.

[7] C. Wurm, O. Oettinger, S. Wittkaemper, R. Zauter, and K. Vuorilehto, "Anode materials for lithium-ion batteries," in *Lithium-Ion Batteries: Basics and Applications* (R. Korthauer, ed.), pp. 43–57, Springer Berlin Heidelberg, 2018.

[8] C. Pillot, "The Rechargeable Battery Market and Main Trends 2011-2020," p. 98, 2017.

[9] Q. Cheng and Y. Zhang, "Multi-Channel Graphite for High-Rate Lithium Ion Battery," *Journal of The Electrochemical Society*, vol. 165, pp. A1104–A1109, Jan. 2018.

[10] M. Yoshio, H. Wang, K. Fukuda, T. Umeno, T. Abe, and Z. Ogumi, "Improvement of natural graphite as a lithium-ion battery anode material, from raw flake to carbon-coated sphere," *Journal of Materials Chemistry*, vol. 14, pp. 1754–1758, May 2004.

[11] M. Kühne, F. Paolucci, J. Popovic, P. M. Ostrovsky, J. Maier, and J. H. Smet, "Ultrafast lithium diffusion in bilayer graphene," *Nature Nanotechnology*, vol. 12, p. nnano.2017.108, June 2017.

[12] K. Persson, V. A. Sethuraman, L. J. Hardwick, Y. Hinuma, Y. S. Meng, A. van der Ven, V. Srinivasan, R. Kostecki, and G. Ceder, "Lithium Diffusion in Graphitic Carbon," *The Journal of Physical Chemistry Letters*, vol. 1, pp. 1176–1180, Apr. 2010.

[13] J. R. Dahn, "Phase diagram of LixC6," *Physical Review B*, vol. 44, pp. 9170–9177, Nov. 1991.

[14] M. S. Dresselhaus and G. Dresselhaus, "Intercalation compounds of graphite," *Advances in Physics*, vol. 30, pp. 139–326, Apr. 1981.

[15] D. Billaud, F. X. Henry, M. Lelaurain, and P. Willmann, "Revisited structures of dense and dilute stage II lithium-graphite intercalation compounds," *Journal of Physics and Chemistry of Solids*, vol. 57, pp. 775–781, June 1996.

[16] N. Daumas and A. Herold, "Sur les relations entre la notion de stade et les mecanismes reactionnels dans les composes d'insertion du graphite," *Comptes rendus de l'Academie des science Serie C*, vol. 268, p. 373, 1969.

[17] E. R. White, J. J. Lodico, and B. C. Regan, "Intercalation events visualized in single microcrystals of graphite," *Nature Communications*, vol. 8, p. 1969, Dec. 2017.

[18] A. M. Dimiev, G. Ceriotti, N. Behabtu, D. Zakhidov, M. Pasquali, R. Saito, and J. M. Tour, "Direct Real-Time Monitoring of Stage Transitions in Graphite Intercalation Compounds," *ACS Nano*, vol. 7, pp. 2773–2780, Mar. 2013.

[19] P. Maire, A. Evans, H. Kaiser, W. Scheifele, and P. Novák, "Colorimetric Determination of Lithium Content in Electrodes of Lithium-Ion Batteries," *Journal of The Electrochemical Society*, vol. 155, pp. A862–A865, Nov. 2008.

[20] D. Billaud and F. X. Henry, "Structural studies of the stage III lithium–graphite intercalation compound," *Solid State Communications*, vol. 124, pp. 299–304, Nov. 2002.

[21] W. Bao, J. Wan, X. Han, X. Cai, H. Zhu, D. Kim, D. Ma, Y. Xu, J. N. Munday, H. D. Drew, M. S. Fuhrer, and L. Hu, "Approaching the limits of transparency and conductivity in graphitic materials through lithium intercalation," *Nature Communications*, vol. 5, p. ncomms5224, July 2014.

[22] F. Grimsmann, T. Gerbert, F. Brauchle, A. Gruhle, J. Parisi, and M. Knipper, "Hysteresis and current dependence of the graphite anode color in a lithium-ion cell and analysis of lithium plating at the cell edge," *Journal of Energy Storage*, vol. 15, pp. 17–22, Feb. 2018.

[23] P. Maire, H. Kaiser, W. Scheifele, and P. Novák, "Colorimetric determination of lithium-ion mobility in graphite composite electrodes," *Journal of Electroanalytical Chemistry*, vol. 644, pp. 127–131, June 2010.

[24] Y. Qi and S. J. Harris, "In Situ Observation of Strains during Lithiation of a Graphite Electrode," *Journal of The Electrochemical Society*, vol. 157, pp. A741–A747, June 2010.

[25] C. Uhlmann, J. Illig, M. Ender, R. Schuster, and E. Ivers-Tiffée, "In situ detection of lithium metal plating on graphite in experimental cells," *Journal of Power Sources*, vol. 279, pp. 428–438, Apr. 2015.

[26] M. Drüe, M. Seyring, and M. Rettenmayr, "Phase formation and microstructure in lithium-carbon intercalation compounds during lithium uptake and release," *Journal of Power Sources*, vol. 353, pp. 58–66, June 2017.

[27] Y. Guo, R. B. Smith, Z. Yu, D. K. Efetov, J. Wang, P. Kim, M. Z. Bazant, and L. E. Brus, "Li Intercalation into Graphite: Direct Optical Imaging and Cahn–Hilliard Reaction Dynamics," *The Journal of Physical Chemistry Letters*, vol. 7, pp. 2151–2156, June 2016.

[28] S. J. Harris, A. Timmons, D. R. Baker, and C. Monroe, "Direct in situ measurements of Li transport in Li-ion battery negative electrodes," *Chemical Physics Letters*, vol. 485, pp. 265–274, Jan. 2010.

[29] J. Zou, C. Sole, N. E. Drewett, M. Velický, and L. J. Hardwick, "In Situ Study of Li Intercalation into Highly Crystalline Graphitic Flakes of Varying Thicknesses," *The Journal of Physical Chemistry Letters*, vol. 7, pp. 4291–4296, Nov. 2016.

[30] J. W. Zondlo, "Graphite: Structure, Properties, and Applications," in *Graphite, Graphene, and Their Polymer Nanocomposites* (P. Mukhopadhyay and R. Gupta, eds.), pp. 1–58, CRC Press, 1st ed., 2012.

[31] X.-G. Yang, G. Zhang, S. Ge, and C.-Y. Wang, "Fast charging of lithium-ion batteries at all temperatures," *Proceedings of the National Academy of Sciences*, vol. 115, pp. 7266–7271, July 2018.

[32] S. Bhattacharya, A. R. Riahi, and A. T. Alpas, "In-situ observations of lithiation/de-lithiation induced graphite damage during electrochemical cycling," *Scripta Materialia*, vol. 64, pp. 165–168, Jan. 2011.

[33] A. Funabiki, M. Inaba, T. Abe, and Z. Ogumi, "Stage Transformation of Lithium-Graphite Intercalation Compounds Caused by Electrochemical Lithium Intercalation," *Journal of The Electrochemical Society*, vol. 146, pp. 2443–2448, July 1999.

[34] M. D. Levi, E. Markevich, and D. Aurbach, "Comparison between Cottrell diffusion and moving boundary models for determination of the chemical diffusion coefficients in ion-insertion electrodes," *Electrochimica Acta*, vol. 51, pp. 98–110, Oct. 2005.

[35] D. A. Porter, K. E. Easterling, and M. Y. Sherif in *Phase Transformations in Metals and Alloys*, pp. 175–184, CRC Press, 3rd, ed ed., 2009.

[36] A. Gilchrist and J. Nobbs, "Colorimetry, Theory," in *Encyclopedia of Spectroscopy and Spectrometry (Third Edition)* (J. C. Lindon, G. E. Tranter, and D. W. Koppenaal, eds.), pp. 328–333, Oxford: Academic Press, 2017.

[37] M. R. Palacín, "Recent advances in rechargeable battery materials: a chemist's perspective," *Chemical Society Reviews*, vol. 38, pp. 2565–2575, Aug. 2009.

[38] Y. Imai and A. Watanabe, "Energetic evaluation of possible stacking structures of Li-intercalation in graphite using a first-principle pseudopotential calculation," *Journal of Alloys and Compounds*, vol. 439, pp. 258–267, July 2007.

[39] K. Toyoura, Y. Koyama, A. Kuwabara, F. Oba, and I. Tanaka, "First-principles approach to chemical diffusion of lithium atoms in a graphite intercalation compound," *Physical Review B*, vol. 78, p. 214303, Dec. 2008.

[40] J. Kalhoff, G. G. Eshetu, D. Bresser, and S. Passerini, "Safer Electrolytes for Lithium-Ion Batteries: State of the Art and Perspectives," *ChemSusChem*, vol. 8, no. 13, pp. 2154–2175, 2015.

Supplementary Materials

Movies S1-5: The movies described in the main text and below can be found on the "UCLA Regan Lab" channel on YouTube.

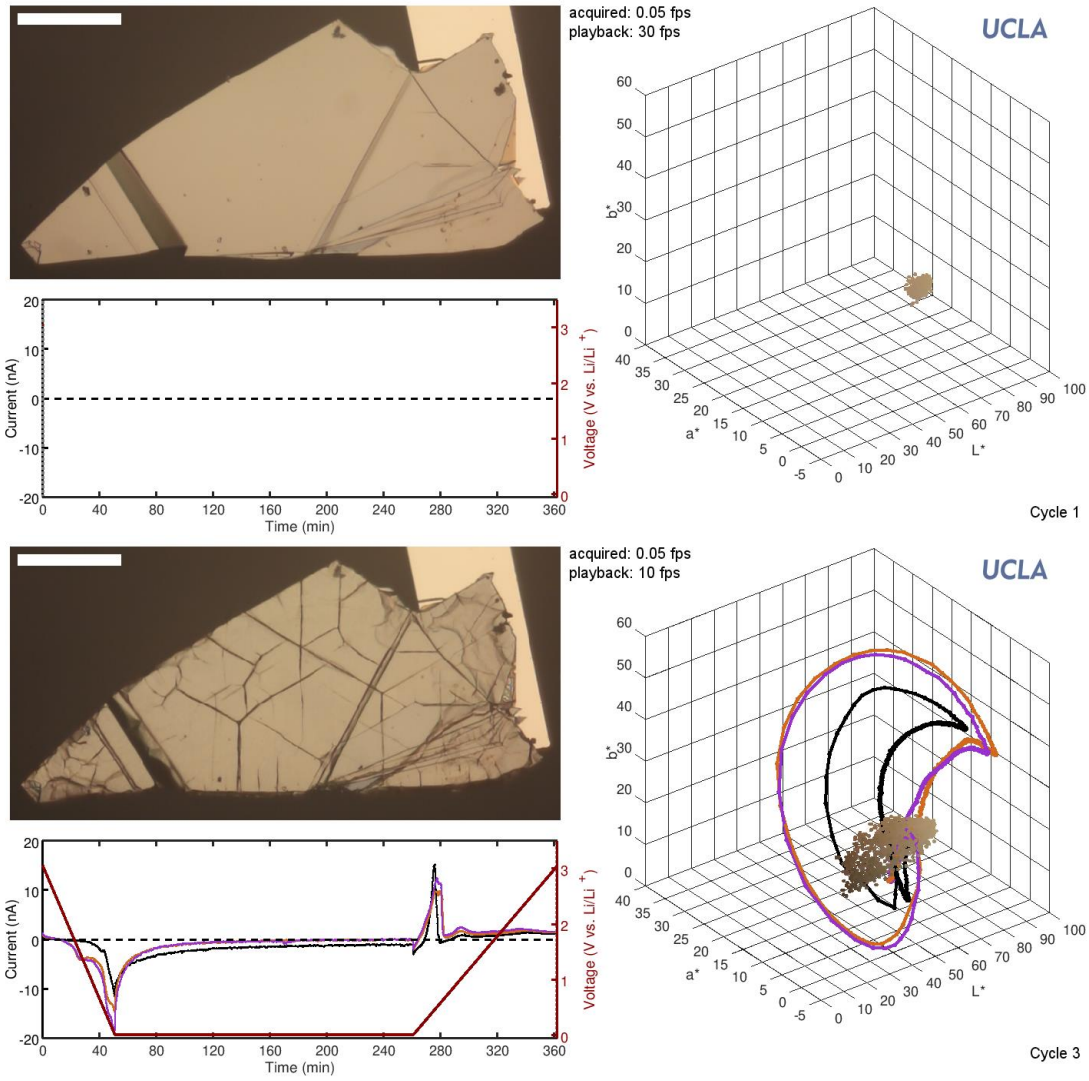

Movie S1. Movie of a single-crystal graphite flake undergoing three lithiation/delithiation cycles. The first (top) and last (bottom) frames are shown above. The optical video, the synchronized electrical transport data, and the L*a*b* color values for pixels within a region of interest (ROI) are shown in the top left, bottom left, and right panels of each frame respectively. In the right panel of each frame the average color for the ROI is also plotted (as a solid line) for each cycle. Here each cycle the potential was ramped from the open circuit potential (OCP), 3.05 V, to 5 mV at -1 mV s^{-1}, held at 5 mV for 3.5 hours, and then returned to the OCP at 0.5 mV s^{-1}. The optical video was acquired at a rate of one frame per 20 seconds. The play-black rates for lithiation and delithiation are 600 × real time and 200 × real time respectively. Both the acquisition and the play-back rates are indicated explicitly in the movie. The scale bar is 50 µm. Still frames and a summary of this experiment are given in Figure 2 of the main text.

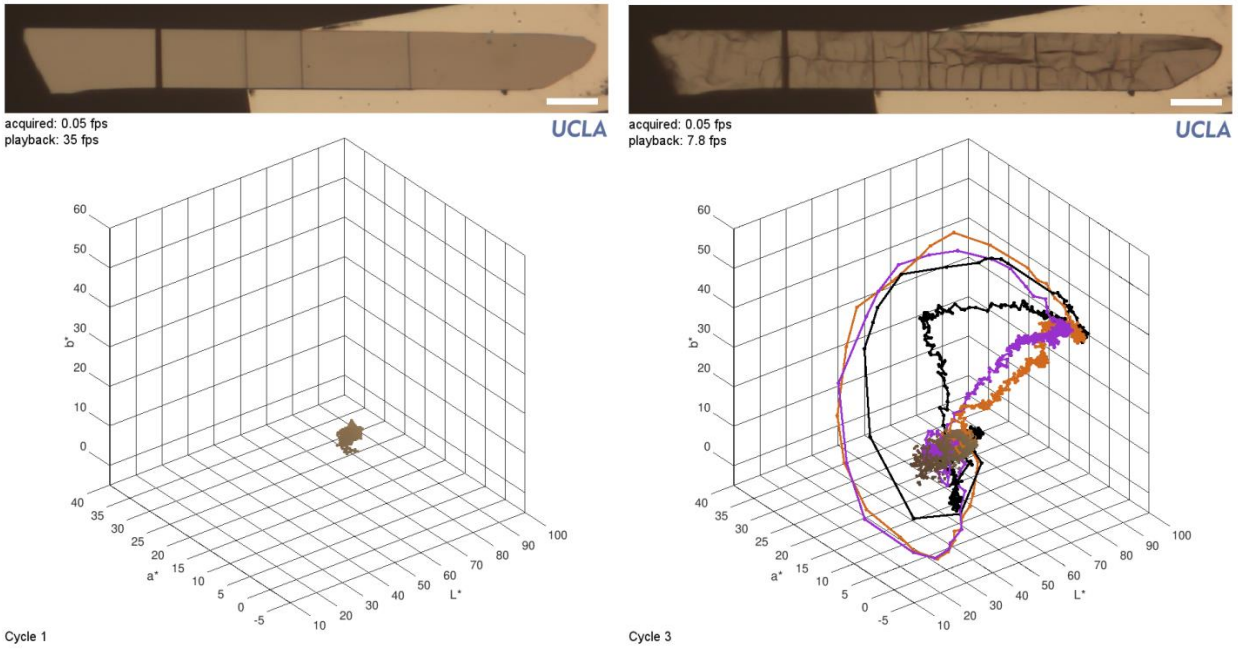

Movie S2. Movie of a single-crystal graphite flake undergoing three lithiation/delithiation cycles. The first (left) and last (right) frames are shown above. The optical video and the L*a*b* color values for pixels within a region of interest (ROI) are shown in the top and bottom panels of each frame respectively. The color trajectory of a single representative pixel (see Supplementary Fig. 11) within the ROI is indicated by a solid colored line. Here each cycle the potential was ramped from the open circuit potential (OCP), 3.22 V, to 5 mV at -1 mV s^{-1}, held at 5 mV for 4 hours, and then returned to the OCP at 0.5 mV s^{-1}. The optical video was acquired at a rate of one frame per 20 seconds. The play-black rates for lithiation and delithiation are 700 × real time and 156 × real time respectively. Both the acquisition and the play-back rates are indicated explicitly in the movie. The scale bar is 20 μm. Still frames and a summary of this experiment are given in Figures 3 and 4 of the main text.

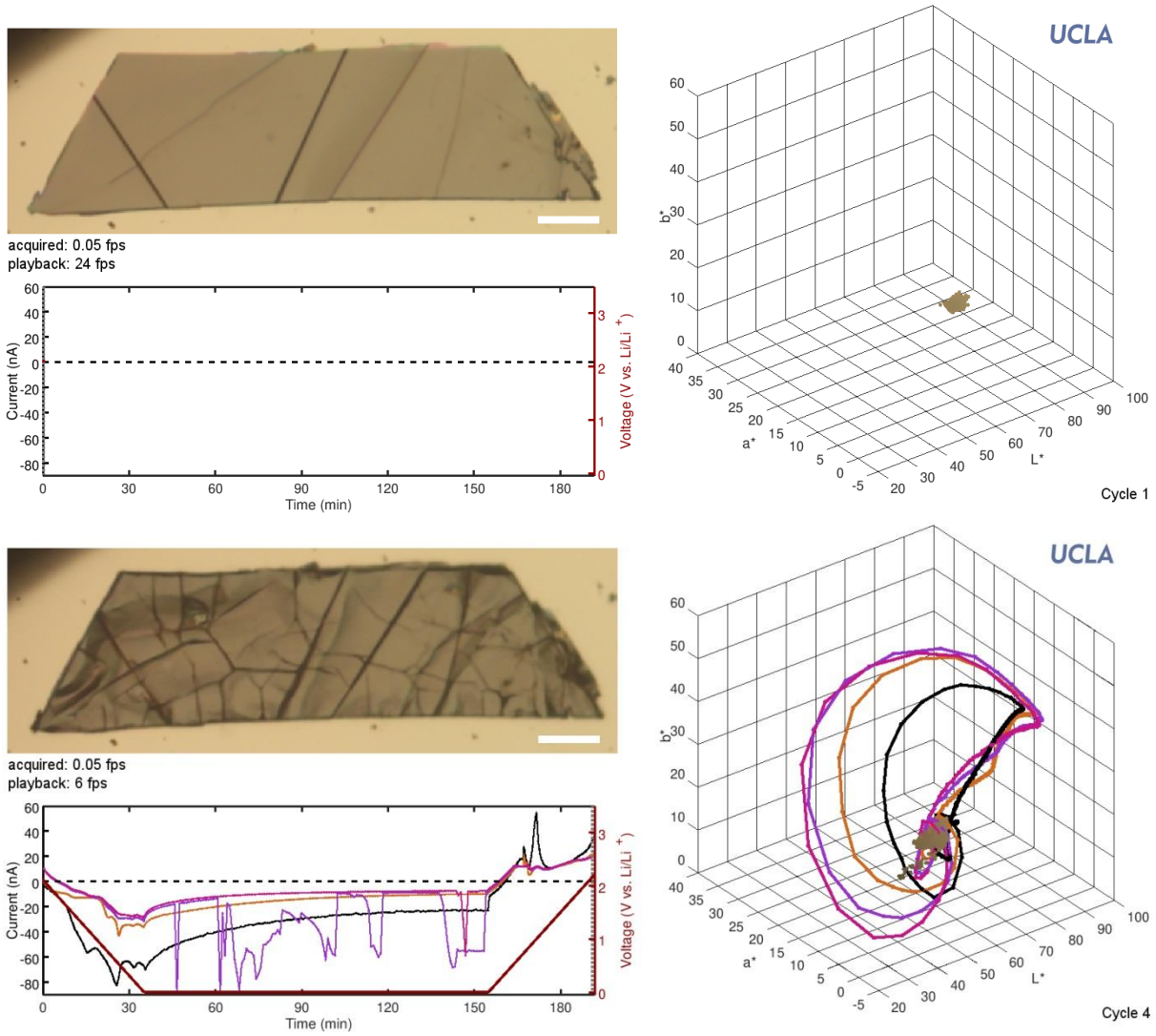

Movie S3. Movie of a single-crystal graphite flake undergoing four lithiation/delithiation cycles. The first (top) and last (bottom) frames are shown above. The optical video, the synchronized electrical transport data, and the L*a*b* color values for pixels within a region of interest (ROI) are shown in the top left, bottom left, and right panels of each frame respectively. In the right panel the average color for the ROI is also plotted (as a solid line) for each cycle. Here each cycle the potential was ramped from the open circuit potential (OCP), 2.2 V, to 5 mV at -1 mV s^{-1}, held at 5 mV for 2 hours, and then returned to the OCP at 1 mV s^{-1}. The optical video was acquired at a rate of one frame per 20 seconds. The play-black rates for lithiation and delithiation are 480 × real time and 120 × real time respectively. Both the acquisition and the play-back rates are indicated explicitly in the movie. We attribute the large current excursions seen in the fourth cycle to background chemical reactions in the SiO_2 (see Figure S2). The scale bar is 20 μm.

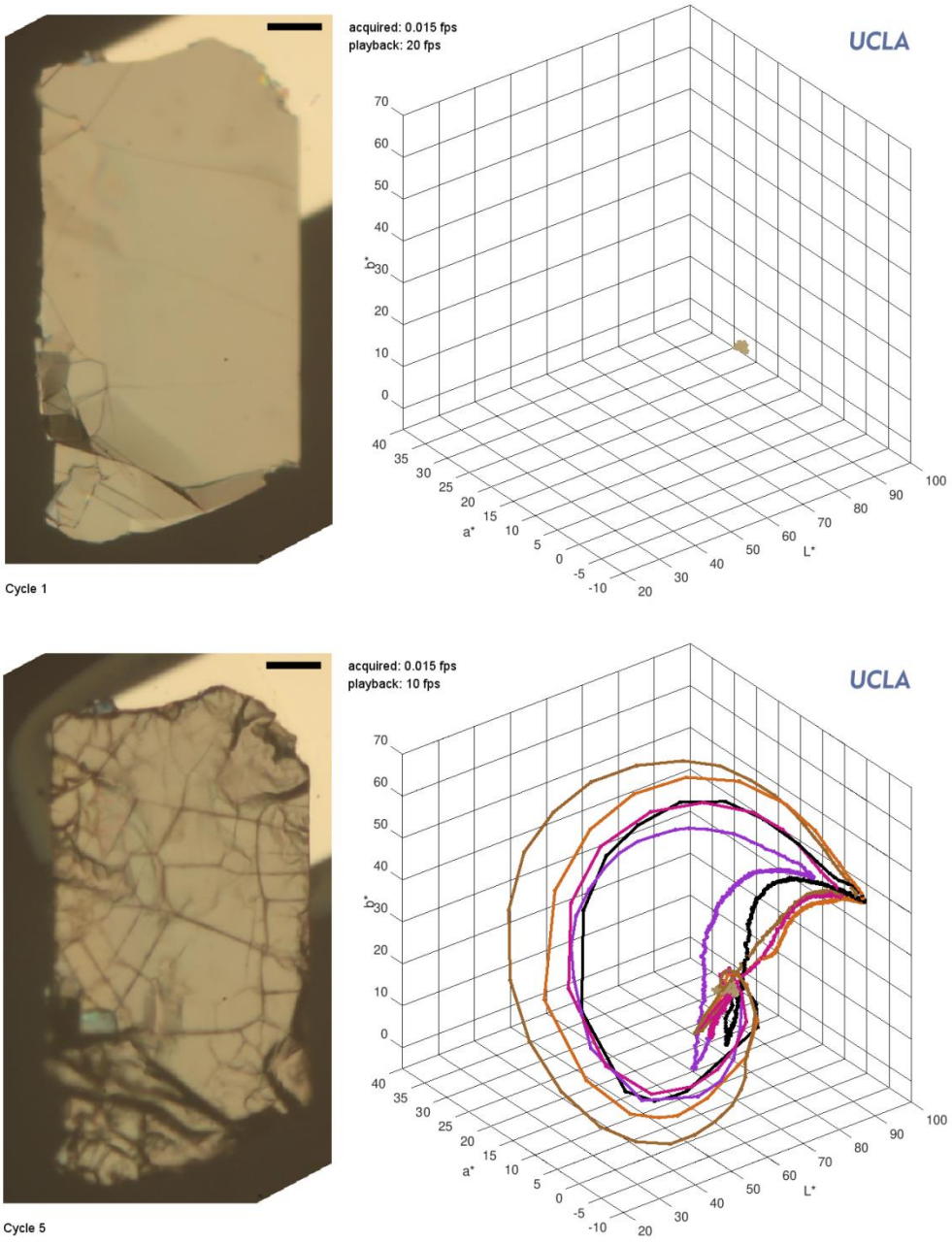

Movie S4. Movie of a single-crystal graphite flake undergoing five lithiation/delithiation cycles. The first (top) and last (bottom) frames are shown above. The optical video and the L*a*b* color values for pixels within a region of interest (ROI) are shown in the left and right panels of each frame respectively. In the right panel the average color for the ROI is also plotted (as a solid line) for each cycle. Here each cycle the potential was ramped from the open circuit potential (OCP), 3.06 V, to 5 mV at -1 mV s^{-1}, held at 5 mV for 3.5 hours, and then returned to the OCP at 1 mV s^{-1}. The optical video was acquired at a rate of one frame per 66.7 seconds. The play-back rates for lithiation and delithiation are 1333 × real time and 667 × real time respectively. Both the acquisition and the play-back rates are indicated explicitly in the movie. The scale bar is 20 µm.

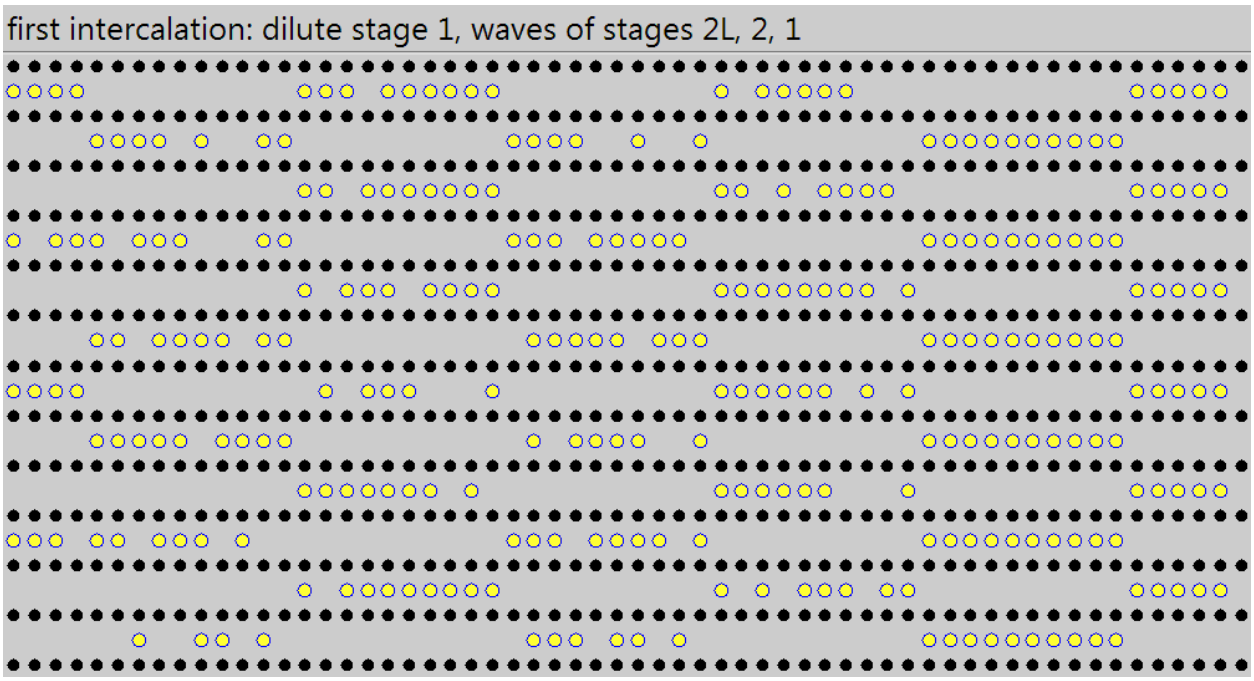

Movie S5. Simulation, generated with National Instruments LabVIEW, showing a cross-sectional view of the lithium kinematics in a section of a graphite crystal during two intercalation/deintercalation cycles. Two modes of intercalation are shown: dilute stage 1 with waves of stages 2L, 2, and 1 (first cycle), and unstaged dilute stage 1 to stage 1 (subsequent cycles). The one mode of deintercalation shown – spatially uniform and staged – is shown, but with two different domain sizes. The black and yellow circles represent carbon and lithium respectively. Still frames and a summary of this simulation are given in Figure 5 of the main text.

Supplementary Figures

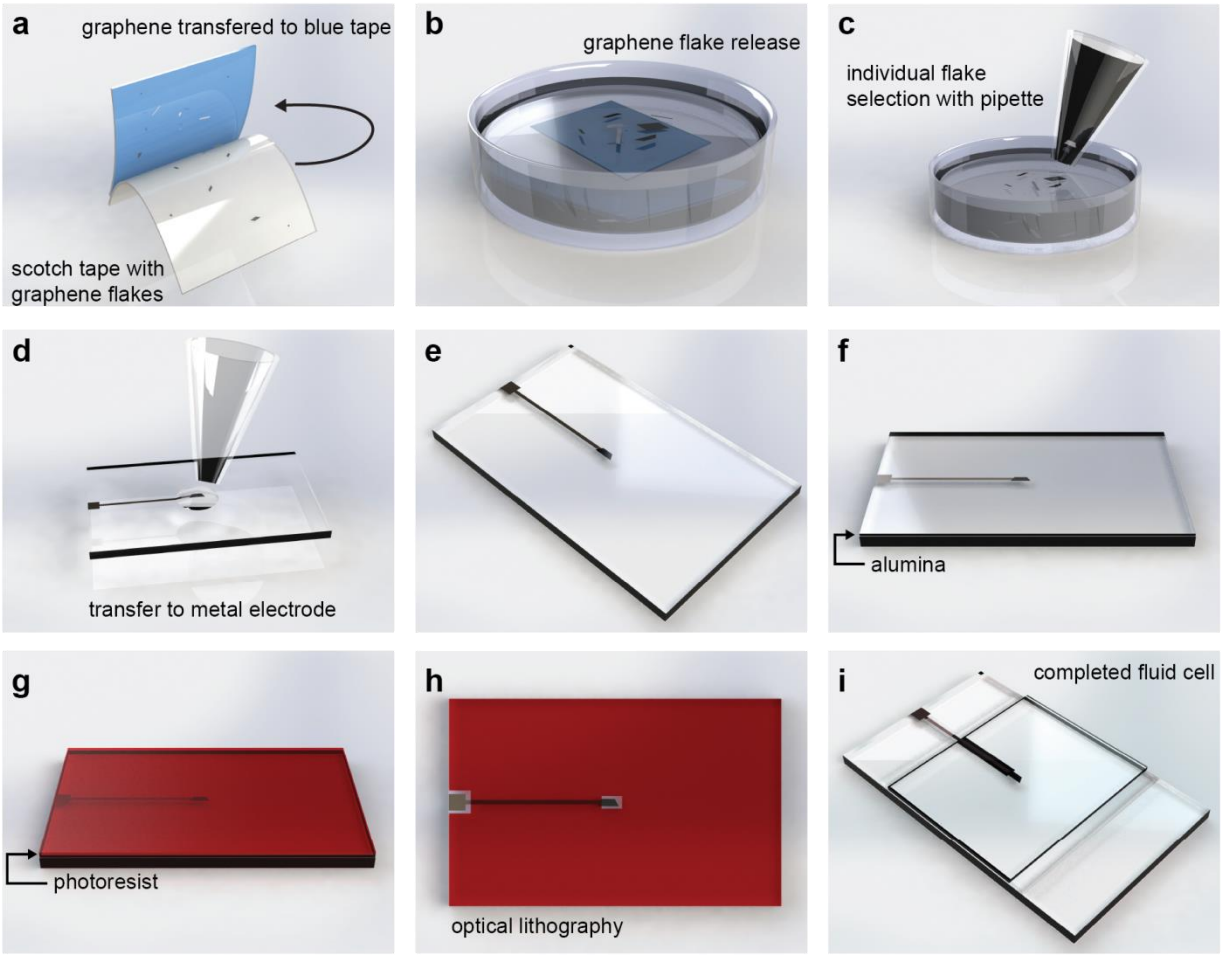

Figure S1. Detailed schematic overview of the pipette-drop transfer process. (**a**) Natural graphite (NGS Naturagraphit GmBH) is exfoliated using Scotch tape and transferred to adhesive blue tape (Loomis Industries, Sec Blue). (**b**) The blue tape and graphite flakes are submerged in acetone, which dissolves the adhesive and thereby releases the graphite. Using a pipette, a single flake is chosen (**c**) and positioned at the tip of a nickel electrode that has been thermally evaporated on a glass slide (**d**). Once the graphite is transferred (**e**) alumina is deposited onto the glass slide via atomic layer deposition (ALD) (**f**). Photoresist (AZ5412) is spun onto the slide (**g**) and optical lithography is used to reveal the graphite and the large pad used for electrical contact (**h**). A buffered oxide etch (BOE) removes the unwanted alumina from the opened areas, and then the remaining photoresist is removed with acetone. Adding a top glass slide to sandwich the graphite and the electrolyte completes the fluid cell (**i**).

	area (μm^2)	thickness (nm)	electrode	# of cycles	figures
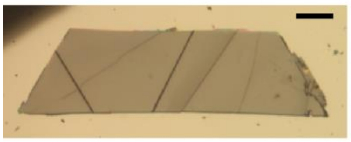	5,250	630	Pt + SiO_2	4	S6
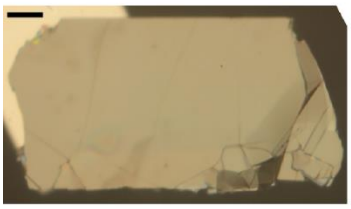	15,180	140	Ni + SiO_2	5	S5, S7b
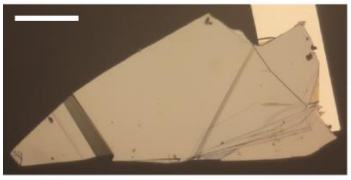	16,790	170	Ni + Al_2O_3	8	2, S3, S7c
	5,070	180	Ni + Al_2O_3	7	3, S4, S8, S9

Figure S2. Table summarizing the graphite flake samples presented. To encapsulate the metal electrode, the first two samples had SiO_2 deposited via thermal evaporation before the graphite was transferred. The SiO_2 was not robust and added significant contributions to the electrical transport (see Movie S3). The Al_2O_3 used for encapsulating the metal electrodes in the second two samples proved to be more successful. (SU-8 might have been an even better alternative, but it was not tried.) The scales bars given in the image of each flake are 20, 20, 50, and 20 μm respectively. Compared to a 20 μm, spherical graphite particle "typical" of a LIB anode, all of these flakes have a smaller volume. However, given that all of the lithium transport occurs in the basal plane, a more relevant comparison is to the square root of the area. By this metric, these flakes are 4 to 6 times larger than typical LIB anode graphite. The 4th flake in this table is exceptional because of its large aspect ratio: its narrow dimension (which is the dimension that matters for determining the charge/discharge time) is ~23 μm, and thus the behavior it shows can be directly compared to that of a typical graphite particle in a LIB anode.

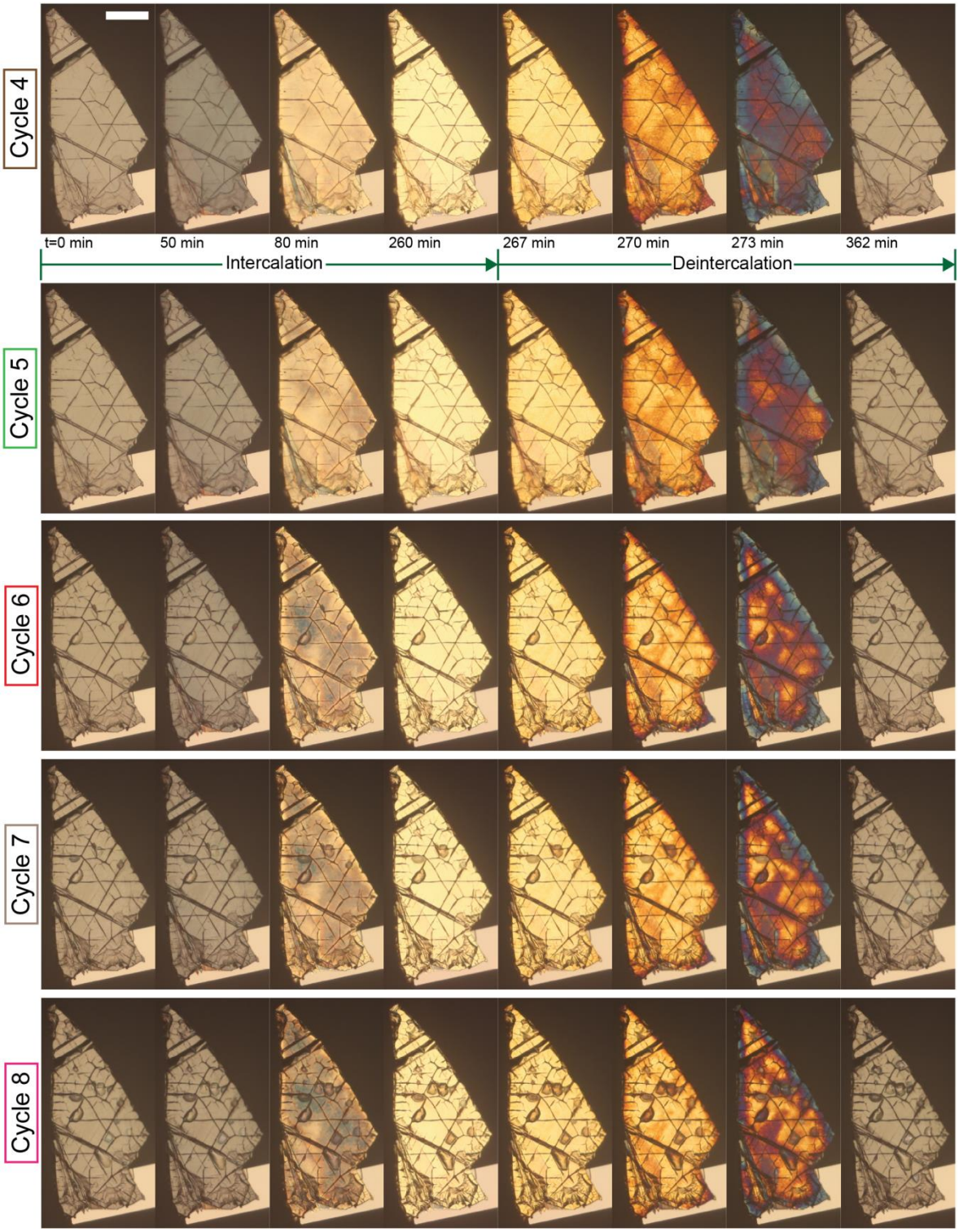

Figure S3. Optical images of the graphite flake in Figure 2 for later cycles. Each cycle shows qualitative color changes similar to cycles 2 and 3. The edge-to-center blue-to-gold color gradient in the 273 minute deintercalation images, and most evident in cycles 6-8, indicates that here the lithium transport within the flake is rate-limiting, as mentioned in the main text. The scale bar is 50 μm and located on the first frame of the first cycle shown.

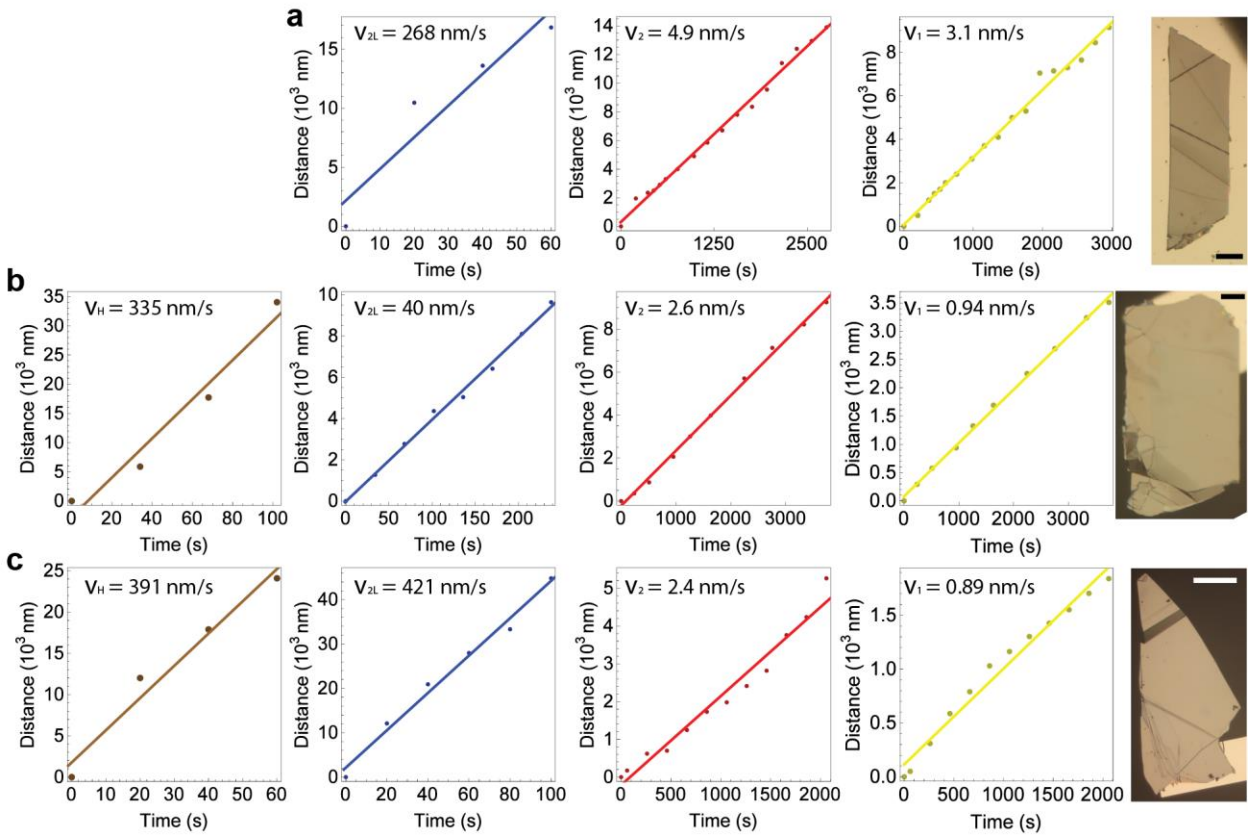

Figure S4. Intercalation wave position vs. time for a specific color. (**a-c**) Each intercalation wave for every flake follows linear trends similar to those of the flake shown in Figure 3. The scale bars in **a**, **b**, and **c** are 20, 20, and 50 μm respectively.

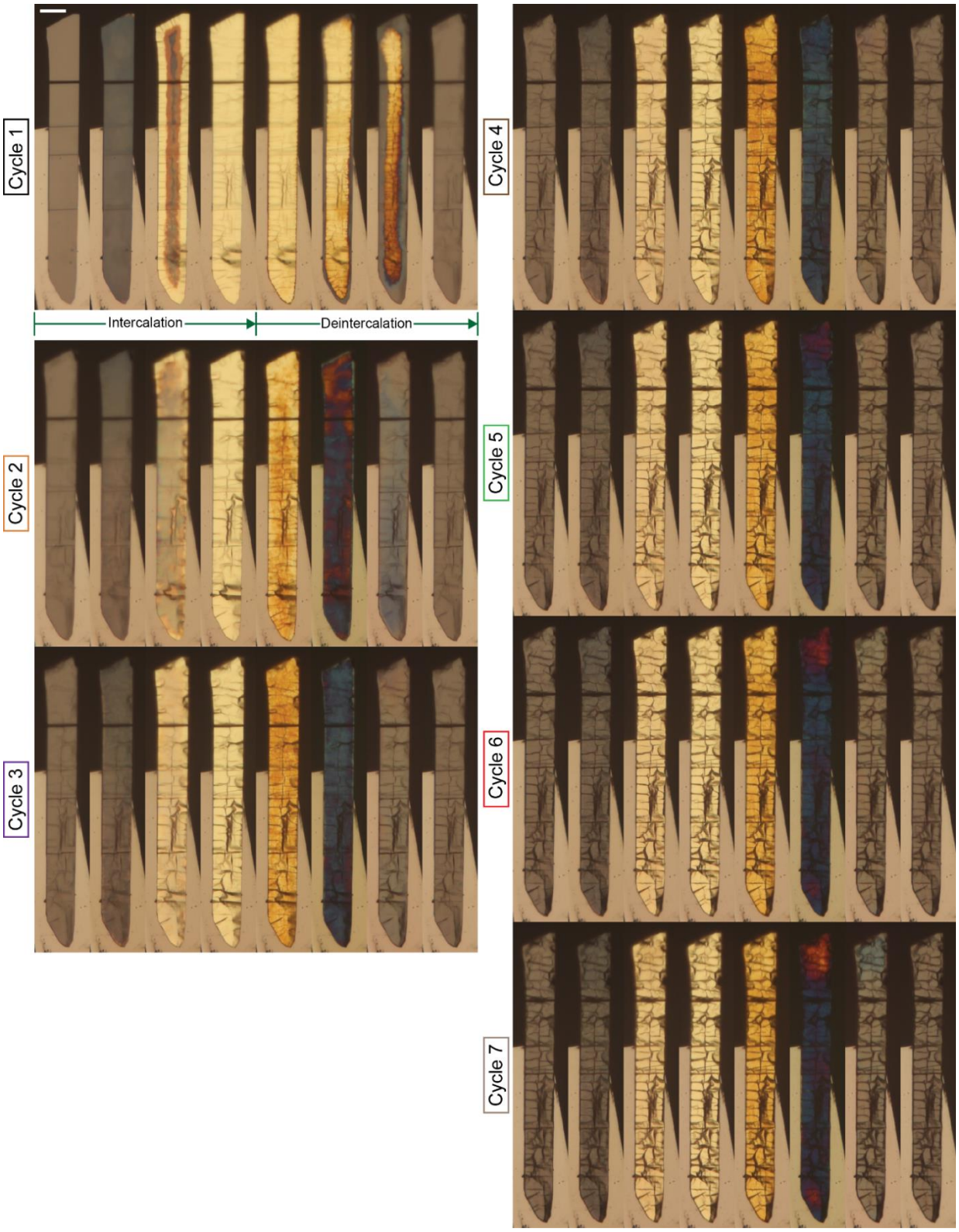

Figure S5. Optical images of the graphite flake in Figure 3 for later cycles. This flake's first deintercalation is exceptional: it shows rate-limiting lithium transport. The scale bar is 20 μm and located on the first frame of the first cycle shown.

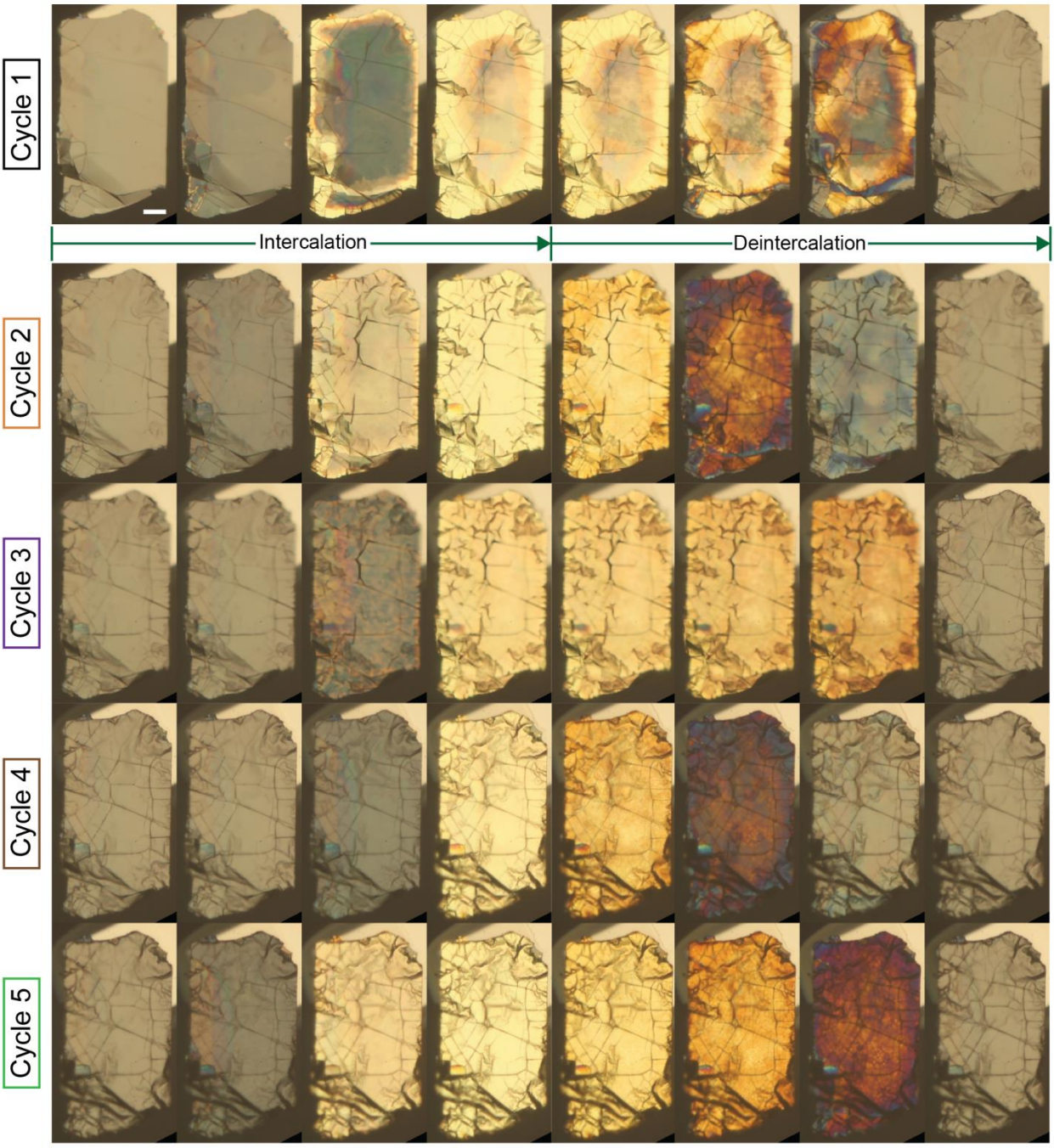

Figure S6. Optical images of a graphite flake from Movie S4 on a nickel electrode covered with SiO_2. In this experiment, the graphite's color is not completely consistent from cycle to cycle. For instance, the deintercalation is delayed in cycle 3, and the intercalation is delayed in cycle 4. We attribute these delays to a poor, intermittent contact between the graphite flake and the metal electrode. At times a bad contact is difficult to identify, especially without high-quality current-voltage data. If the parasitic currents are large, the best indication of a broken connection might be that the sample color ceases to follow the electrode potential, as in the main data of ref. 27 of the main text. The scale bar is 20 μm and located on the first frame of the first cycle shown.

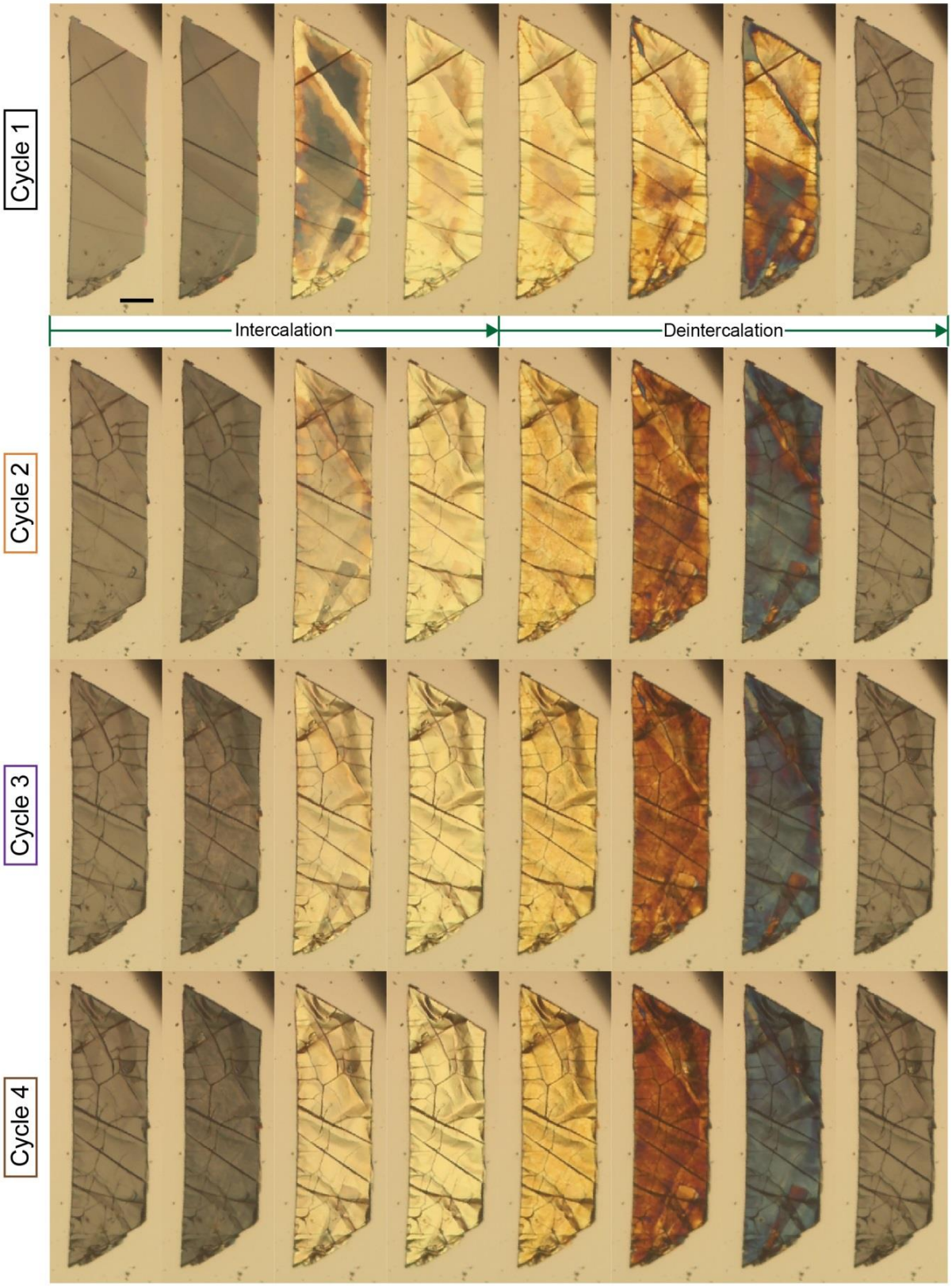

Figure S7. Still images of the graphite flake in Movie S3. As with all of the other samples, the first cycle is markedly different from all others, and the color trajectories for intercalation are not

the time-reverse of those for deintercalation. Because the interior angles of this trapezoidal flake are multiples of 60°, it is possible that its prismatic faces are predominantly either armchair or zigzag. A flake that had two long, straight edges joined by either a 30° or a 90° corner would allow one to visualize differences in the lithium ion transport intercalating from armchair or zigzag edges. Unfortunately none of the flakes studied here have the required geometry. The scale bar is 20 μm and located on the first frame of the first cycle shown.

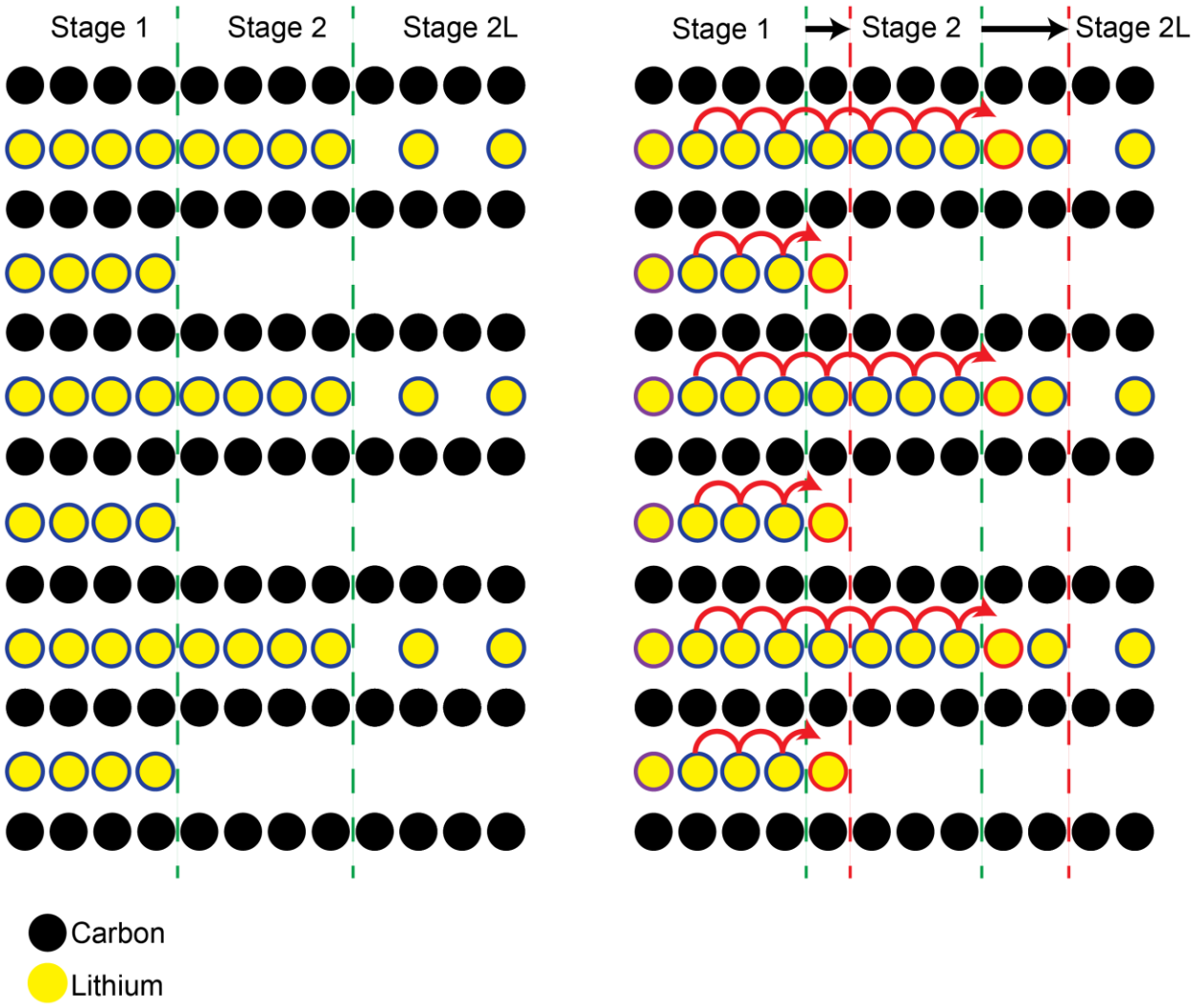

Figure S8. Cross sectional view of a simplified model of the first intercalation. (left) The partially intercalated graphite flake has three distinct phases (1, 2, and 2L), shown separated by a green dashed line in the initial state. (right) Intercalating lithium ions uniformly (one per graphene layer, purple outline, 6 ions total) advances previously intercalated (blue outline) ions to the right (red arrows). Here, the net number of ions in phase 1, 2, and 2L increased by 6, 3, and -3, respectively. Because the 2L phase is less dense than the 2 phase, uniform intercalation moves the 2-2L phase boundary faster than it moves the 1-2 phase boundary (red dashed lines and black arrows).

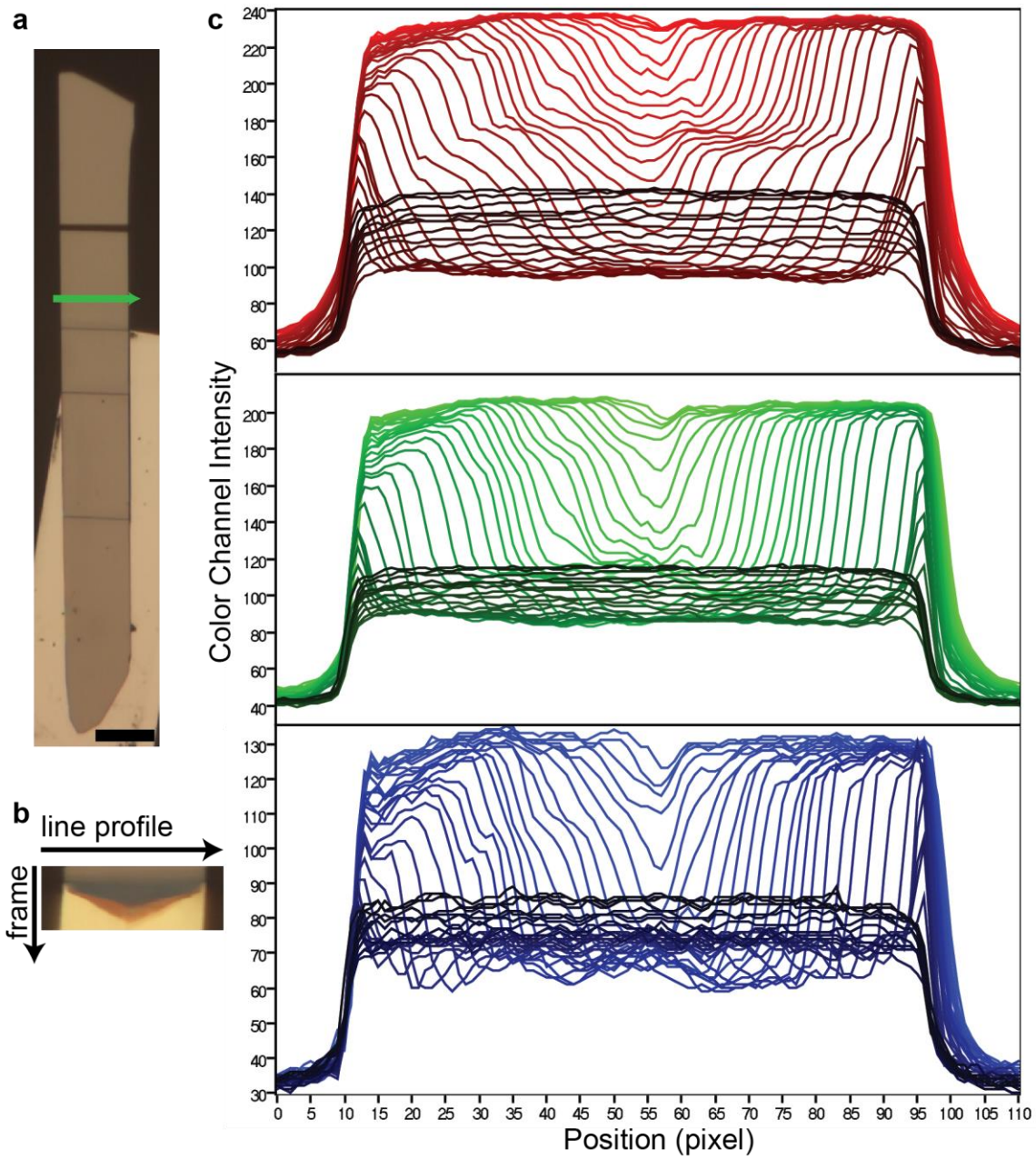

Figure S9. (**a**) A still image from Movie S2. Line profiles extracted from the position of the green arrow in 39 frames from the first intercalation cycle are combined to form (**b**) and three waterfall plots for each raw RGB color channel (**c**). In (c) the profiles progress from black (first frame) to red, green, and blue (last frame), respectively. The first frame was taken at 1 V vs Li/Li^+, before any intercalation was observed. The following 15 start 14.7 min from the first and are evenly separated by 20 s. The next 22 are equally spaced 200 s from each other. The final frame, acquired 103 min after the first, shows the highest intensity in all three channels. See Figure S12 for a single-frame view of the staircase-like structures shown here. The scale bar in (a) is 20 μm. A pixel is 260 nm on a side.

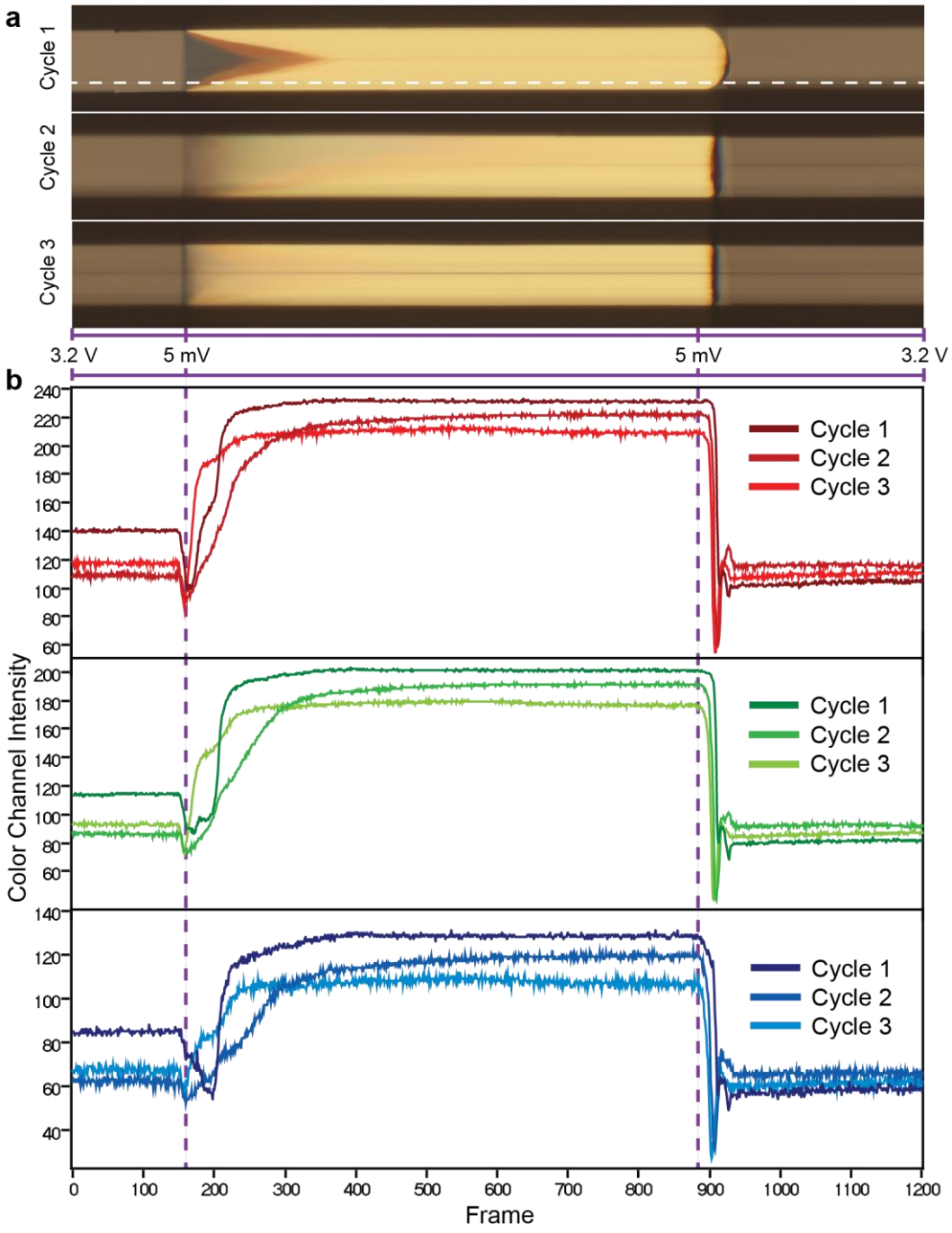

Figure S10. (**a**) Space-time slice of the first three lithiation/delithiation cycles. Movie S2 shows 2D (*x,y*) color maps as a function of time *t*. Here we display 2D (*t, y*) color maps. Each column here is a single-pixel column extracted from each frame in Movie S2 at the position indicated by the green arrow in Fig S9a. The three-phase coexistence and their constant velocity phase wavefronts are clearly seen in the first cycle, but absent in the following two cycles. The raw, unprocessed red, green, and blue (RGB) values for the dashed line profile in (a) is shown in (**b**) for all three cycles.

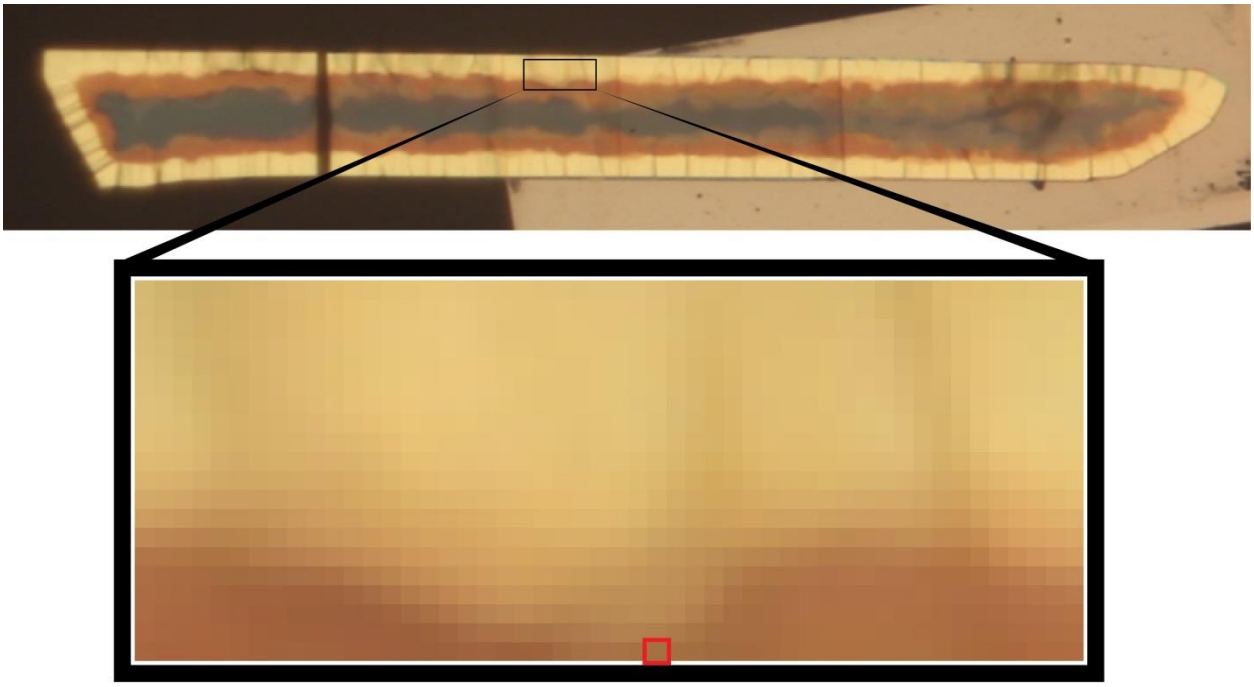

Figure S11. A still frame from Movie S2 (see caption) highlighting the 50 pixel × 20 pixel ROI (black box) and the representative pixel (red box).

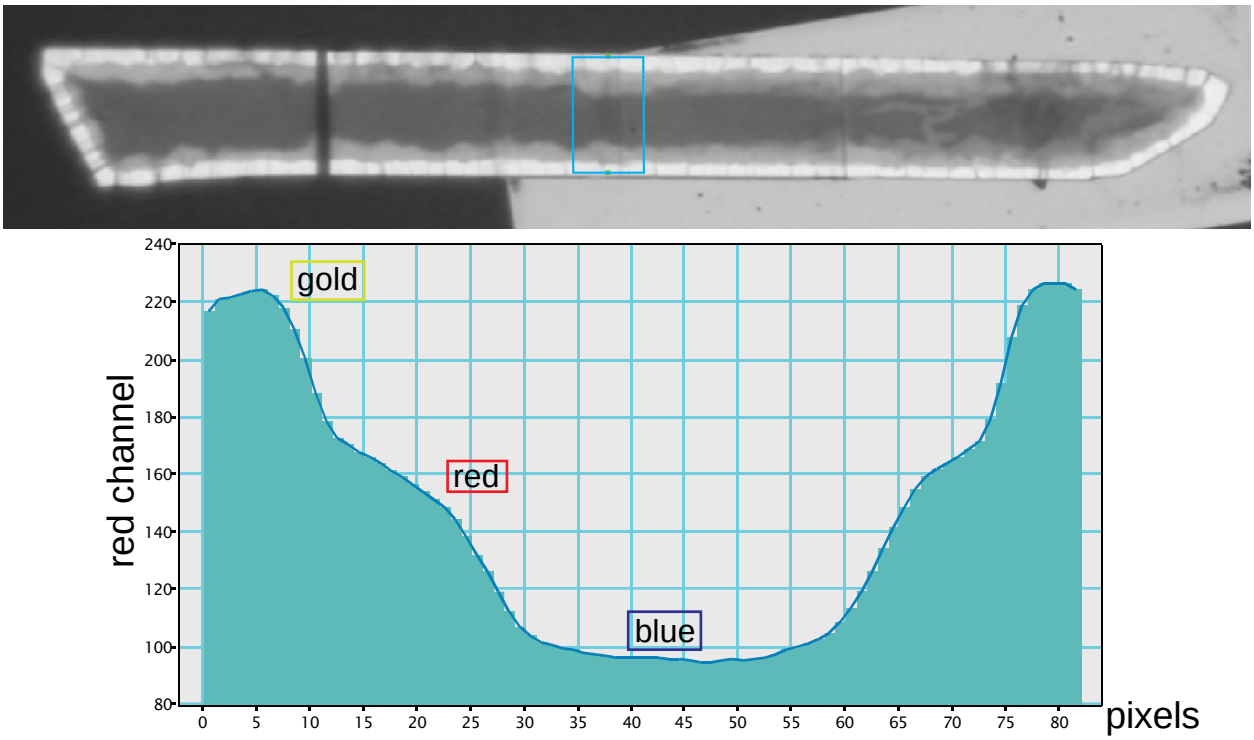

Figure S12. A still image (top) from Movie S2. The blue box (50 x 82 pixels) shows the averaged line profile that is plotted (bottom). If color can be taken as a proxy for concentration, these profiles are inconsistent with simple, Fickian diffusion. The choice of the red channel for display is arbitrary – similar profiles are seen in the green and blue color channels (not shown).

Diffusion coefficient discussion.

To ease comparison with previous work, we give order-of-magnitude estimates for some effective diffusion coefficients. Dimensional analysis shows $D \simeq v \times d$, where v is the wavefront velocity and d is a length scale corresponding to the local curvature in the concentration profile. Taking $d \sim 700$ nm, our optical resolution, gives $D \sim (1\text{-}3)\times 10^{-11}$ cm^2/s for the red-to-gold phase transition, and $D \sim (2\text{-}5)\times 10^{-11}$ cm^2/s for the blue-to-red phase transition. (High stage transitions show D about a hundred times larger.) These values are somewhat small[1–4] and apply only to the first lithiation; for all subsequent lithiations (and delithiations) these 'diffusion constants' have increased to such an extent that they can no longer be estimated using this method. Note, however, the dangers of this approach. If the concentration profile is, in fact, staircase-like (we think this likely), then the lithium ion transport is not diffusion-limited. And regardless of whether the concentration gradient is truly step-like or merely unresolved, the 'diffusion coefficient' calculated by the imputed concentration gradient reflects only the spatial resolution of the observing apparatus.[4]

References

(1) Park, M.; Zhang, X.; Chung, M.; Less, G. B.; Sastry, A. M. A Review of Conduction Phenomena in Li-Ion Batteries. *J. Power Sources* **2010**, *195* (24), 7904–7929. https://doi.org/10.1016/j.jpowsour.2010.06.060.

(2) Persson, K.; Sethuraman, V. A.; Hardwick, L. J.; Hinuma, Y.; Meng, Y. S.; van der Ven, A.; Srinivasan, V.; Kostecki, R.; Ceder, G. Lithium Diffusion in Graphitic Carbon. *J. Phys. Chem. Lett.* **2010**, *1* (8), 1176–1180. https://doi.org/10.1021/jz100188d.

(3) Kühne, M.; Paolucci, F.; Popovic, J.; Ostrovsky, P. M.; Maier, J.; Smet, J. H. Ultrafast Lithium Diffusion in Bilayer Graphene. *Nat. Nanotechnol.* **2017**, *12* (9), nnano.2017.108. https://doi.org/10.1038/nnano.2017.108.

(4) Maire, P.; Kaiser, H.; Scheifele, W.; Novák, P. Colorimetric Determination of Lithium-Ion Mobility in Graphite Composite Electrodes. *J. Electroanal. Chem.* **2010**, *644* (2), 127–131. https://doi.org/10.1016/j.jelechem.2009.09.011.